Using co-located radars and instruments to analyse ionospheric events over South Africa

A thesis submitted in partial fulfillment of the
requirements for the degree of

MASTER OF SCIENCE

of

Rhodes University

by

Racheal Athieno

July 2011

Abstract

Space weather and its effect on technological systems are important for scientific research. Developing an understanding of the behaviour, sources and effects of ionospheric events form a basis for improving space weather prediction. This thesis attempts to use co-located radars and instruments for the analysis of ionospheric events over South Africa. The HF Doppler radar, ionosonde, Global Positioning System (GPS) and GPS ionospheric scintillation monitor (GISTM) receivers are co-located in Hermanus (34.4° S, 19.2° E), one of the observatories for the space science directorate of the South African National Space Agency (SANSA). Data was obtained from these radars and instruments and analysed for ionospheric events. Only the Hermanus station was selected for this analysis, because it is currently the only South African station that hosts all the mentioned radars and instruments. Ionospheric events identified include wave-like structures, Doppler spread, sudden frequency deviations and ionospheric oscillations associated with geomagnetic pulsations. For the purpose of this work, ionospheric events are defined as any unusual structures observed on the received signal and inferred from observations made by the HF Doppler radar. They were identified by visual inspection of the Doppler shift spectrograms. The magnitude and nature of the events vary, depending on their source and were observed by all, some or one instrument. This study suggests that the inclusion of a wider data coverage and more stations in South Africa merit consideration, especially since plans are underway to host a co-located radar network similar to that in Hermanus at at least three additional observatory sites in South Africa. This study lays a foundation for multi-station co-located radar and instrument observation and analysis of ionospheric events which should enhance the accuracy of space weather and HF communication prediction.

Acknowledgements

I wish to extend my sincere gratitude to my supervisor, Dr. Lee-Anne Mckinnell, for her guidance, motivation and continued support throughout the entire period of this study. Sincere gratitude to Dr. Jaroslav Chum for his time and assistance in understanding the Doppler data. Thanks to Dr. Ben Opperman and Dr. Pierre Cilliers for the tireless guidance and help in understanding the GPS data. Thanks to Dr. John Bosco Habarulema for his continuous advice, guidance and assistance.

I appreciate the financial assistance and support provided by the SANSA Space Science staff and the entire community for hosting me and creating a conducive, positive environment during my study. I am also grateful to National Astrophysics and Space Science Programme (NASSP) for all the financial support provided. I am grateful to Nkanyiso Mbatha and Chigomezyo Ngwira for their assistance in introducing and nurturing me to the MATLAB world. Thanks to my friends Emirant, Electdom, Mpho for their contribution and all fellow SANSA students who supported and encouraged me in any way.

Special thanks to my mother, brothers, sister for the love, care, financial support and for being by my side all through my study time. May the almighty God bless you all. The patience, love, care, financial and moral support of Mr. Kayizzi Godfrey is highly appreciated.

Glory be to the Almighty God for His everlasting love, provision and for the far He has brought me, “EBENEZER”.

Contents

List of Tables

List of Figures

Chapter 1

Introduction

This thesis aims to investigate the use of co-located radars and instruments to analyse ionospheric events of various origins, including adverse space weather. The radars used were a high frequency (HF) Doppler radar and ionosonde. The other instruments used in the analysis include Global Positioning System (GPS) receiver, GPS ionospheric scintillation total electron content (TEC) monitor (GISTM) and magnetometer.

The GPS receiver and GISTM receive radio signals from GPS satellites while the HF Doppler radar and the ionosonde use a network of transmitters and receivers to provide real-time data on sky wave propagation (Sizun, 2005). Sky wave propagation involves reflection and refraction of the transmitted radio signals from the ionosphere. The ionosphere (the part of the atmosphere between altitudes of about 50 km to 1 000 km) is able to reflect and refract radio waves which forms the basis for HF propagation over long distances. The propagation and reception of radio signals by means of these radars are affected by the ionosphere due to its unstable nature. Thus the term "ionospheric events" may simply be perceived as the effect of the ionosphere on the radio signals transmitted or received by the co-located radars and instruments.

1.1 Objectives and relevancy of the study

Several authors have observed and discussed ionospheric events (e.g. Hines, 1960; Georges, 1968; Šauli *et al.*, 2006; Laštovička, 2006; Chum *et al.*, 2008). Event analysis has mostly been done by either using a single radar or a number of radars located at different observatory sites. This study offers the first ionospheric event analysis of data from a co-located radar network in Africa. The results demonstrate the use of co-located radars and instruments to study and enhance our understanding of ionospheric events and thus the accuracy of space weather and HF communication prediction. In particular, the results of this study will facilitate the choice of frequencies for international short wave broadcasters, radio navigation and the operation of radar systems. The specific objectives of this study are to

- Identify ionospheric signatures, such as wave-like structures and Doppler spread signal from Doppler shift spectrograms;
- Identify correlations between Doppler radar signatures and signatures on the other co-located radars and instruments;
- Investigate the possible mechanisms responsible for these signatures using multiple radar data sources.

In 2007, the South African National Space Agency (SANSA) Space Science directorate (previously the Hermanus Magnetic Observatory) received a mandate from the International Space Environment Service (ISES) to operate a Regional Warning Center (RWC) for space weather prediction in Africa. This research will contribute to the output of the RWC, as well as significantly expanding the knowledge base for future research.

1.2 Thesis overview

The ionospheric events referred to in this study are any unusual signatures/structures observed on the signal received by the different radar receivers. The data used in this analysis was recorded by the co-located radars and instruments at SANSA Space Science located in Hermanus (34.4° S, 19.2° E). The radars and instruments

at SANSA Space Science include a HF Doppler radar, ionosonde, GPS receiver, GISTM and magnetometer. The analysed events are attributed to a reflection from a moving or sporadic layer and small irregularities in the ionosphere. The changes in the reflection layer are a consequence of various factors including changes in the neutral atmosphere and its constituents. The changes in the neutral atmosphere result from the tendency of the atmosphere to retain its equilibrium state against the forces of imbalance, due to differences in pressure, temperature or density. In this study, a spectral analysis was done on the signal recieved from the HF Doppler radar to obtain Doppler shift spectrograms which were manually checked for ionospheric events. An event analysis involved looking for correlations between Doppler radar signatures and signatures on other co-located radars and instruments. It also involved finding a probable mechanism responsible for the observed signatures by looking at the space and terrestrial weather conditions at the time of the event, using parameters such as solar wind speed, geomagnetic indices and terrestrial wind speed.

This thesis consists of five chapters. Chapter 1 includes a brief introduction about the topic, objectives and relevancy of the study and thesis overview. The theoretical background is covered in Chapter 2. A brief description of the instruments and radars involved in the study and data analysis techniques is covered in Chapter 3. Chapter 4 offers the results and their discussion. Chapter 5 contains concluding remarks and recommendations for future work.

Chapter 2

Theoretical background

2.1 Introduction

This study investigates the use of co-located radars and instruments to study ionospheric events over South Africa. This was done by transmitting radio signals into space and analysing the signal received by the radars. The ionospheric events are then inferred from the analysis of the received signal. It is therefore important to understand the Earth's atmosphere and ionosphere as the medium for radio propagation. A knowledge of radio propagation is also important. This chapter offers a brief introduction to the Earth's atmosphere and a detailed description of the ionosphere and its influence on high frequency (HF) propagation. Included is a brief description of the effect of space weather on HF propagation.

2.2 The Earth's atmosphere

The Earth's atmosphere is a layer that surrounds planet Earth and is retained by the Earth's gravitational field. This gravitational field is mainly responsible for making the atmosphere heterogeneous and the propagation of atmospheric waves anisotropic. Throughout the atmosphere temperature varies with altitude, and the different regions are characterised by density, temperature, composition, degree of ionisation and motion. Various natural or artificial phenomena which may result from the different forms of energy and physical mechanisms present in the atmosphere occur in and/or propagate through the atmosphere. Such phenomena may be meteorological, optical (e.g. reflection and refraction), acoustical (sound

wave propagation), chemical, electric or magnetic. Some of these phenomena may be oscillatory or turbulent (Sizun, 2005).

The two main regions of the atmosphere are the homosphere and heterosphere.

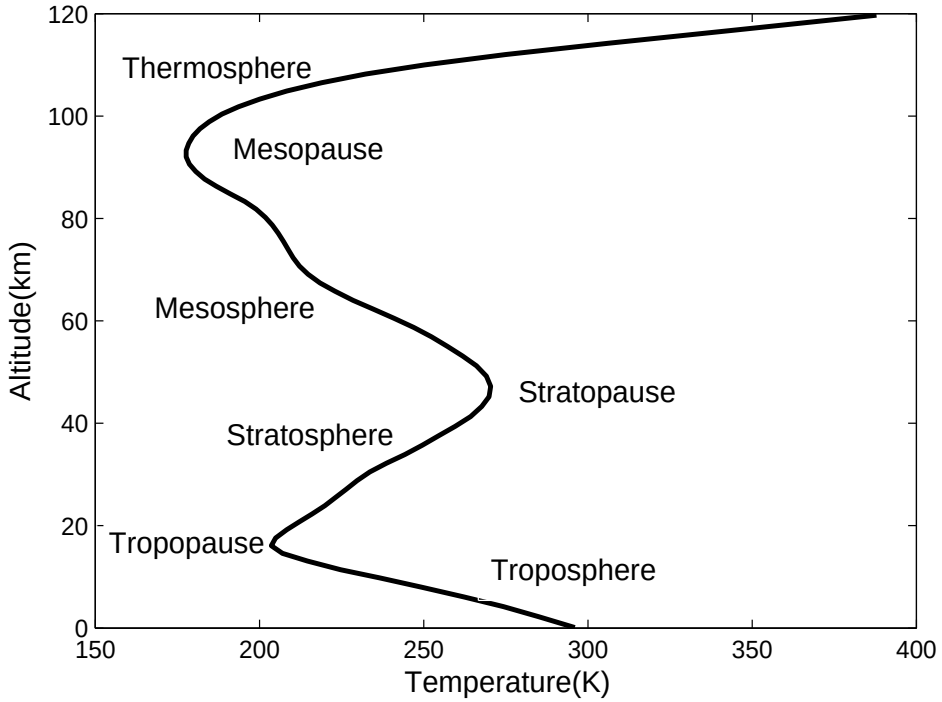

Figure 2.1: The atmospheric temperature profile as a function of the altitude (plotted using CIRA86 model data).

The homosphere consists of the troposphere, stratosphere and mesosphere and extends from the Earth's surface up to $\sim$ 80 km. Beyond the homosphere is the heterosphere which consists of the thermosphere and the exosphere. These regions are usually represented by a temperature profile as shown in figure 2.1. The troposphere is the lowest layer of the atmosphere and it extends to about 10 km. Depending on various conditions such as geographical latitude and meteorological activity, this altitude varies between 8 km at the poles and 18 km at the equator. The regular decrease in temperature with an increase in altitude characterises this layer, which makes up 85 percent of the total mass of the atmosphere, with molecular nitrogen (N_2), molecular oxygen (O_2) and argon (Ar) being its major constituents. This layer is also known to be the origin of most of the meteoro-

logical phenomena, including the formation of clouds, and is subdivided into the turbulent layer and the free atmosphere. The turbulent layer extends from the surface up to an altitude of 1 500 metres over plains, and to higher altitudes over high-relief areas. Mechanical or thermal interactions between the terrestrial surface and the atmosphere happen in the turbulent layer (Sizun, 2005).

Beyond the tropopause is the stratosphere. The temperature in the stratosphere slowly increases up to a maximum of 290 K at an altitude of $\sim$ 50 km. This increase in temperature is due to the absorption of a part of the ultraviolet radiation emitted by the Sun. The stratosphere therefore forms a regulating filter which creates the conditions for existance of life on Earth. It is the area where aeroplanes fly (at $\sim$ 10 km) and it contains the ozone layer (Sizun, 2005).

The mesosphere lies above the stratopause and is a region of decreasing temperature with a minimum found at about 85 km. The thermosphere lies above the mesosphere and is made up of mainly atomic oxygen. Its temperature increases with altitude up to the thermopause. Above the thermosphere is the exosphere which extends to altitudes higher than 1 000 km. Its major constituents are hydrogen and helium.

2.3 The ionosphere

The ionosphere is an ionised part of the atmosphere that lies between altitudes of about 50 km and 1 000 km. It falls within the mesosphere and thermosphere and consists of three regions, namely the lower ionosphere (between 50 km and 90 km), the bottomside ionosphere (between 90 km and about 350 km) and the topside ionosphere (between about 350 km and 1 000 km). The ionosphere is formed when solar extreme ultra violet (EUV) radiation interacts with the atoms and molecules in the neutral atmosphere by a process known as photoionisation. The process of photoionisation may be expressed (Rishbeth and Garriot, 1969) as

$$N_{atom} + h\nu \longrightarrow N^{+}_{atom} + e^{-} \tag{2.1}$$

where N_{atom} is the neutral atom or molecule and $h\nu$ is the photon flux. The ionosphere derives its name from the ions formed during photoionisation, but the interest lies in the freely moving and lighter electrons, because their increasing density causes refraction of radio waves and therefore are significant for HF propagation (McNamara, 1990). The basic theory of ionisation is described by the Chapman function which gives the rate of ion production. The Chapman theory

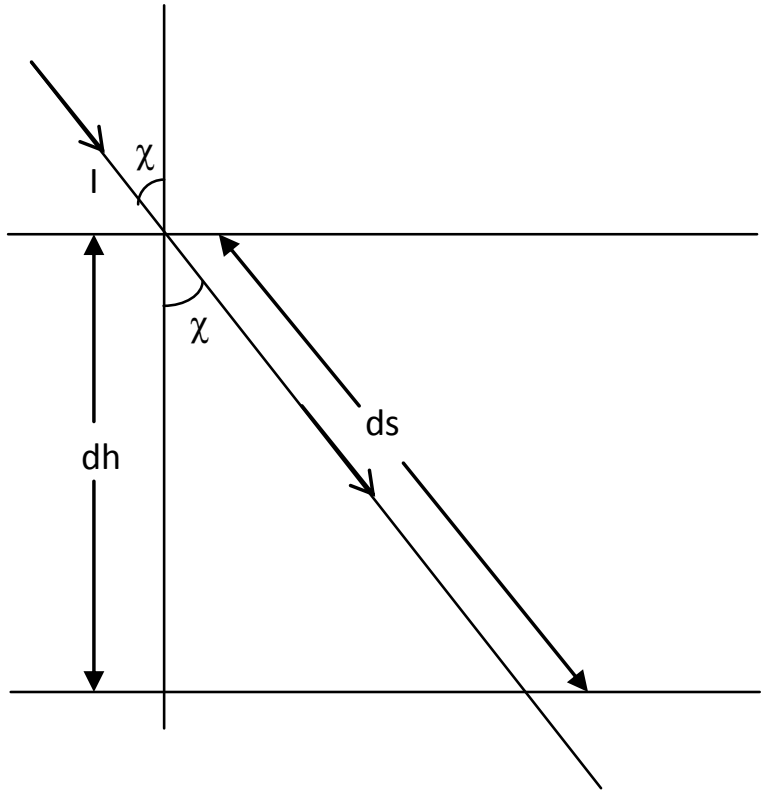

Figure 2.2: Diagram to illustrate the basic theory of ionisation. Adopted from Rishbeth and Garriot (1969).

assumes that solar ionising radiation is monochromatic and attenuates as it traverses a horizontally stratified layer as shown in figure 2.2 (Rishbeth and Garriot, 1969). The solar ionising radiation, I (photons m^2s^{-1}) incident at an angle, χ to the atmosphere decreases as it travels through the distance, ds, mainly due to absorption. The Chapman function in simplified terms is given (Rishbeth and Garriot, 1969; Davies, 1989) by

$$q(z, \chi) = q_0 exp[1 - z - sec\chi e^{-z}] \tag{2.2}$$

where

$$z = \frac{(h - h_0)}{H_p}$$

H_p is the pressure scale height, h_0 and q_0 are the reference height and rate of ion production at $z = 0$ respectively and χ is the solar zenith angle. The peak ion production rate is obtained by differentiating equation 2.2,

$$q_m = q_0 cos\chi \tag{2.3}$$

and is the rate of ion production when the sun is overhead, i.e. at $\chi = 0$.

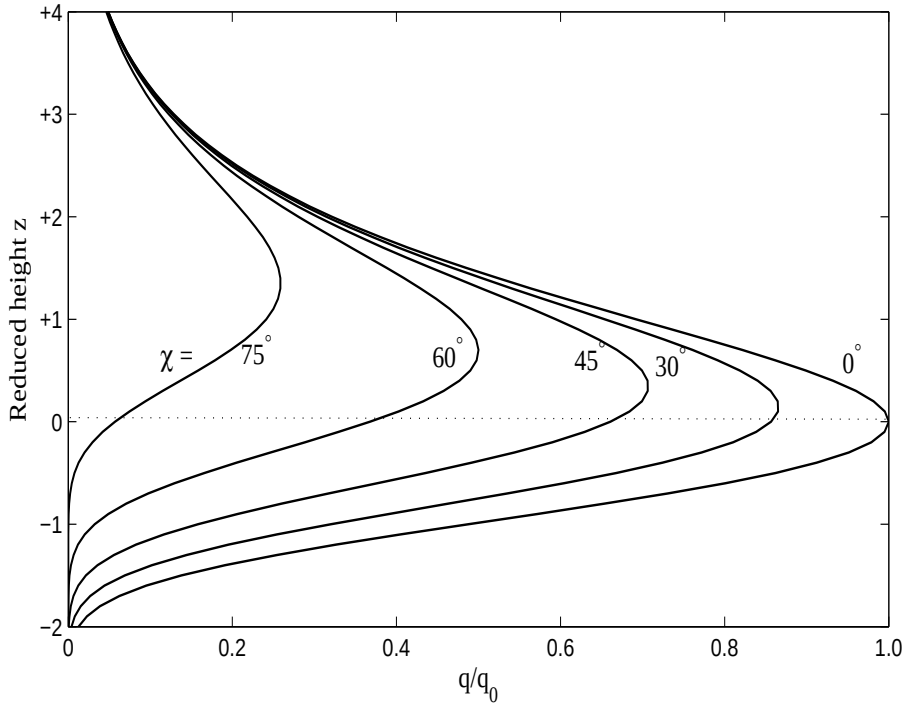

Figure 2.3: Variation of $\frac{q}{q_0}$ with z. Courtesy of C. Ngwira (2011) who adopted it from Rishbeth and Garriot (1969).

Figure 2.3 shows how $\frac{q}{q_0}$ changes with z for selected values of χ. It is clear that the rate of ion production is greatest at $z = 0$ when $\chi = 0°$. Thus, the electron density is greatest at/ close to midday when the sun is overhead ($\chi = 0°$). When solar radiation is incident on the neutral atmosphere as illustrated in figure 2.2, the density of the neutral atmosphere increases downwards while the solar radiation

intensity decreases due to absorption. Thus, the ionisation rate decreases due to the depletion of the photons even though the density of the ionisable neutral atmosphere increases (Rishbeth and Garriot, 1969). The peak ion production occurs at a height where the rate of decrease in the radiation intensity balances with the increase in the density of the ionisable neutral atmosphere. Below the peak value, there is a significant drop in the rate of ion production. Looking at figure 2.3, the region above $z = 0$ is that part of the curve where the effect due to the increase in the neutral density is dominant, i.e. $|z|>>|e^{-z}sec\chi|$ in equation 2.2. The region below $z = 0$ is where the effect due to increasing optical depth, $\tau = e^{-z}sec\chi$ and decreasing solar radiation intensity, i.e. $|e^{-z}sec\chi|>>|z|$ are dominant. Considering figure 2.2, the path length of the photons, ds, is given by

$$ds = -dhsec\chi \tag{2.4}$$

ds is proportional to $sec\chi$ and therefore increases with increasing solar zenith angle, χ. This implies that an increase in χ makes the term $|e^{-z}sec\chi|>>|z|$ in equation 2.2 to be dominant which leads to a decrease in the ion production rate, $\frac{q}{q_0}$. Thus the rate of ion production is inversely proportional to the increase in the solar zenith angle (Rishbeth and Garriot, 1969). This explains the variation of the ion production rate at various solar zenith angles observed in figure 2.3.

The ionosphere is important for radio communication because of its natural ability to reflect radio waves (McNamara, 1990). It is a doubly refracting medium for the propagation of radio waves owing to the presence of the earth's magnetic field. Radio wave propagation is described by the Appleton-Hartree equation which after neglecting collisions is simplified (Rishbeth and Garriot, 1969; Davies, 1989) as,

$$n^2 = 1 - \frac{X(1-X)}{(1-X) - \frac{1}{2}Y_T^2 \pm \{\frac{1}{4}Y_T^4 + (1-X)^2Y_L^2\}^{\frac{1}{2}}} \tag{2.5}$$

where

$$X = \frac{\omega_p^2}{\omega^2},\ \ Y = \frac{\omega_g}{\omega},\ \ Y_L = Ycos\theta,\ \ Y_T = Ysin\theta,\ \ \omega_p^2 = \frac{N_e e^2}{m_e \varepsilon_0},\ \ \omega_g = \frac{Be}{m_e}$$

n is the refractive index, N_e, e, m_e are the electron density, charge and mass respectively, ε_0 is the permittivity of free space, B is the flux density of the geomagnetic

field. θ is the angle between the direction of propagation of the radio wave and the magnetic field (Rishbeth and Garriot, 1969). f is frequency of the radio wave, f_p is the plasma frequency and f_g is the gyrofrequency. The + and - signs describe the propagation of the ordinary (O-) and extraordinary (X-) waves respectively. If the radio wave propagates in the same direction as the magnetic field, i.e. $\theta = 0$, it implies that $Y_L = Y$ and $Y_T = 0$ (Rishbeth and Garriot, 1969) and equation 2.2 reduces to

$$n^2 = 1 - \frac{X}{(1 \pm Y)} \tag{2.6}$$

Neglecting the effect of the magnetic field on the propagation of radio waves (by setting $B = 0$) for the sake of simplicity implies that $\omega_g = 0$, $Y = 0$ and equation 2.3 becomes

$$n^2 = 1 - X = 1 - \frac{\omega_p^2}{\omega^2} \tag{2.7}$$

where the angular plasma frequency, ω_p is given by

$$\omega_p = 2\pi f_p \tag{2.8}$$

and $\omega = 2\pi f$ is the angular frequency of the radio wave.
Thus, the index of refraction, n, at frequency f is given by

$$n^2 = 1 - \frac{f_p^2}{f^2} = 1 - \frac{e^2 N}{4\pi^2 \epsilon_0 m_e f^2} \tag{2.9}$$

which is a much more simplified form of the Appleton-Hartree equation.
Squaring both sides of equation 2.8 and substituting for ω_p^2,

$$\omega_p^2 = (2\pi f_p)^2$$

$$\frac{N_e e^2}{m_e \varepsilon_0} = (2\pi f_p)^2$$

$$N_e = \left(\frac{2\pi m_e \varepsilon_0}{e^2}\right)^2 f_p^2$$

Substituting for $m_e = 9.11 \times 10^{-31}$ kg, $\varepsilon_0 = 8.854 \times 10^{-12}$ Fm^{-1} and $|e| = 1.602 \times 10^{-19}$ yields

$$N_e = 1.24 \times 10^{10} f_p^2 \tag{2.10}$$

which is the equation that relates the electron density to the plasma frequency (Davies, 1989; McNamara, 1990). Ionospheric behaviour is affected by a number of factors, including solar activity and the Earth's magnetic field. The ionosphere is not a stable ionised medium, and its variations can strongly affect HF propagation. Sudden occurrence of strong disturbances (associated to solar activity) in the ionosphere may interrupt HF communication in a given band of frequency (McNamara, 1990; Sizun, 2005).

2.3.1 Regions of the ionosphere

The lower and bottomside ionosphere is made up of three regions of varying electron densities and altitude, namely: the D, E, and F layers. These regions are formed by photoionisation and their variation is dependent on factors such as time of the day, solar activity and season. The F region is subdivided into two regions: F1 and F2 depending on the ionisation levels.

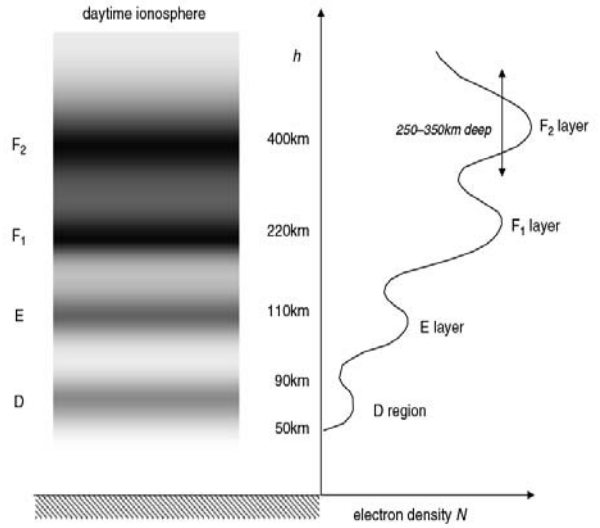

(a)

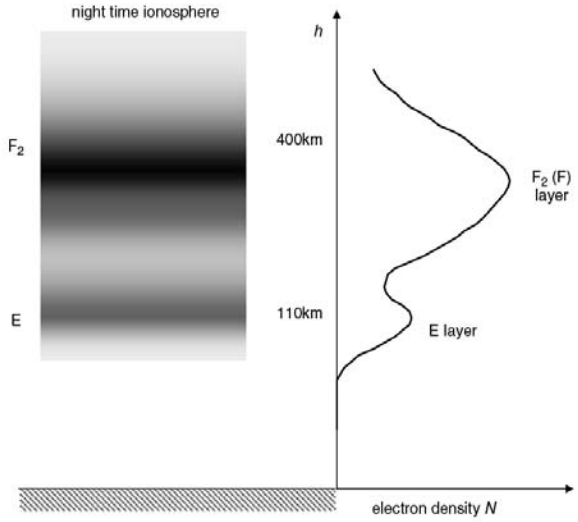

(b)

Figure 2.4: (a) Typical daytime and (b) nighttime ionosphere. Darker shading represents higher electron densities (Richards, 2008).

As shown in figure 2.4, all the layers are present during the day due to photoionisation, but during the night some layers disappear mainly as a result of the recombination process. For each of these layers, there exists a critical frequency which corresponds to the peak electron density of that particular layer (see equation 2.10).

The D region

The D-region is the lowest region of the ionosphere and lies within the range of about 70 - 90 km. However, to account for the contribution of galactic cosmic rays in the region that lies between 50 - 70 km (C-region), its lower boundary is usually placed at 50 km. Ion production in the D region is mainly due to solar x-rays or Lyman ionisation of nitrogen oxide (NO) (McNamara, 1990; Goodman, 2005). Being at a lower altitude, the D region molecules are squeezed closer together by gravity than those in the higher layers, and the free electrons reattach to the molecules easily. This region is important in the characterisation of absorption losses for short wave systems and as a reflecting layer for long wave communication and very low frequency (VLF) waves and navigation systems (Goodman, 2005). The greatest level of absorption of radio waves is found in this layer. Radio waves at lower frequencies cannot penetrate this layer and are absorbed. The higher frequency signals are able to pass through the D layer. During solar flares, the D layer becomes ionised so strongly that all HF radio waves are absorbed, causing a radio blackout.

The E region

This region lies between 90 - 120 km above the Earth's surface. Ion production during the day is due to the ionisation of molecular (O_2) and atomic (O) oxygen and during the night to electron and meteor bombardment. During the day it reflects HF waves up to 20 MHz which is only applicable for oblique propagation (McNamara, 1990; Goodman, 2005).

The F region

The F region is the maximum electron density region and lies between approximately 120 - 350 km. Ion production in this layer is due to ionisation of atomic oxygen (O) by Lyman continuum or emission lines of helium (He) (McNamara, 1990). During the daytime, especially in summer, the F region splits up into two separate regions F1 and F2. The F2 region is the most important region for HF propagation, because its free electrons have the longest lifetime. This allows the F2 region to survive throughout the night and to reflect the highest frequencies in the HF range (McNamara, 1990; Baumjohann and Treumann, 1997). The critical

frequency of the F2 region, denoted by foF2, is a measure of the variation in the peak electron density in the ionosphere. The F2 region is also known to exhibit anomalies. One of them is the seasonal or winter anomaly, when the winter values of noon peak electron density strongly exceed those of summer (Millward *et al.*, 1996).

2.3.2 Regular ionospheric variations

Diurnal variations

The ionosphere varies with the time of the day. Since photoionisation varies with solar radiation, the electron density is greatest at local midday when the sun is overhead. At sunset, photoionisation stops and the electrons are depleted by recombination (a process by which electrons and ions combine to produce neutral atoms) (McNamara, 1990). The electron density decreases as the night wears on causing the D, E and F1 regions to disappear. The F2 layer is present at night due to the fact that the effective recombination rate decreases with increasing height. Therefore, communication during the night is mainly by the F2 region, except in the presence of a sporadic layer. Through the night, maximum frequencies gradually decrease reaching their minimum just before dawn (McNamara, 1990).

Solar activity variations

Since solar radiation is responsible for the formation of the ionosphere, solar activity such as solar flares affect the ionosphere, which in turn affect HF propagation. An increase in solar activity increases the electron density which allows the use of higher frequencies. Thus, at solar maximum, the higher frequencies will successfully propagate while at solar minimum, the ionosphere reflects lower frequencies in the HF band (Goodman, 2005). This solar activity is usually measured using sunspots or the 10.7 cm solar radio flux index (F10.7). The sunspot number varies with an 11-year solar cycle during which periods of solar minimum and solar maximum are observed. Observations show that the ionospheric electron density is greater during the solar maximum than solar minimum (McNamara, 1990).

Latitudinal variations

The ionosphere also varies with latitude and season due to the change in the neutral atmosphere and variation in the solar zenith angle. The intensity of the solar radiation, and hence the production of electrons, decreases with increasing latitude (McNamara, 1990).

Seasonal variation

The critical frequencies of the D, E and F1 regions are greater in summer than in winter due to the position of the sun. The F2-layer is known to exhibit an anomalous behaviour relating to the seasonal variation in the midday peak electron density (Millward *et al.*, 1996). The winter values of noon peak electron density are much greater than those in summer, a phenomenon known as the seasonal or winter anomaly (Croom *et al.*, 1960; Zandt and Knecht, 1964). A knowledge of seasonal variation is important for determining the suitable frequencies to be used in radio communication.

2.3.3 Irregular ionospheric variations

Irregular ionospheric variations are unpredictable and have a great impact on HF propagation. The common irregular variations include sporadic E, spread F, sudden ionospheric disturbances and ionospheric storms.

Sporadic E (Es) layer

The Es layer is an irregular layer which to a lesser extent is directly influenced by the radiation emitted by the Sun. It can be envisaged as plasma clouds in suspension within the E layer, and refers to the largely unpredictable formation of regions of very high electron density in the E region which may form at any time of the day. High frequencies meant for the F layer can be reflected by the Es layer (if foEs $\gtrsim$ foF2). The foEs for a given location can vary from $2-3$ MHz to more than 30 MHz. It is a daytime and summer phenomenon at low and mid-latitudes, while mostly prevailing during the nighttime at high latitudes. There exists a blanketing frequency (fbEs) below which Es is opaque and above which it is transparent to the passage of radio waves to the F region. In some cases, the

radio wave may be partially reflected by the Es layer and F layer which may result in irregular signal transmission or fading (Davies, 1989). Es may be associated with thunderstorms, meteor showers, solar activity, and geomagnetic activity. For mid-latitudes, sporadic E layers are formed via the so-called "$V \times B$" (V and B are the neutral wind and magnetic field vectors, respectively) or "windshear" mechanism (Whitehead, 1989).

Spread F

Spread F is as a result of diffusion of the F region due to scattering of the radio wave, reflection from ionospheric plasma irregularities and travelling ionospheric disturbances (TIDs). It tends to occur when there is a reduction in the F region electron density (decrease in foF2) and is therefore associated with ionospheric storms (Davies, 1989). The radio waves transmitted are often reflected from different heights in the ionosphere at slightly different times and therefore the received signal is the superposition of such waves. The transmitted pulse often has a much shorter duration than the echo pulse reflected from the F layer. Spread F is a nighttime phenomenon at low latitudes (around the equinoxes). The likelihood of occurrence of Spread F at mid-latitudes is less compared to low and high latitudes and spread F is most likely to occur at night and in winter. Spread F can be either frequency spread, which refers to diffuseness near the critical frequency of the F2 layer, or range spread, which refers to diffuseness near the horizontal part of the trace (Davies, 1989).

Ionospheric storms

Ionospheric storms are associated with a number of phenomena, including solar activity and geomagnetic, auroral and magnetospheric storms. Ionospheric storms are known to affect ionospheric characteristics such as the electron density or the height of the F2 layer. They can cause an increase in the virtual height of the F2 layer and a decrease in the maximum electron density which may interrupt radio communication. In most cases, the lower layers are affected when the disturbance is great. These storms may affect human technology e.g. cause outages in electric power systems and increase of atmospheric drag on satellites (Davies, 1989; Sizun, 2005).

2.4 High frequency (HF) propagation

HF propagation involves transmission and reception of radio signals within a frequency range of $3 - 30$ MHz. The four principal modes of radio wave propagation are free-space waves, sky waves, tropospheric waves and ground waves. Free-space waves propagate from point-to-point by the most direct path and are only affected by distance. Sky waves are influenced by the ionosphere. Tropospheric waves are affected by variations in the structure of the refractive index of the air through which they traverse. Ground waves refer to the propagation of radio waves either close to or at the surface of the Earth and their attenuation depends on antenna height, polarisation, frequency, ground types, terrain and/or sea state (Dennison and Lorek, 2005).

2.4.1 Sky wave propagation

Sky wave propagation is the propagation of radio signals from one point to another after reflection by the ionosphere and is a consequence of total internal reflection of the radio waves. The electron density increases with altitude and the refractive index decreases. Hence, as the radio signal penetrates the ionosphere it travels from a dense to a less dense medium, continuously bending away from its path until the signal suffers total internal reflection back to the Earth. The characterisitics of a radio wave are subject to change on penetration of the ionosphere due to factors such as the state of the ionosphere, the frequency, transmitter power and the take-off angle relative to the ground. The frequency of the transmitted signal is a very important factor in radio wave propagation. A wave transmitted at a given frequency may either be reflected back to a receiver by the ionosphere or may just penetrate through the ionosphere. The wave may also be absorbed along its path due to collisions between the charged and neutral particles. However, the frequency of the received wave may be slightly different (shifted) from the transmitted wave due to movement of the reflection layer. The amplitude and phase of the received radio wave may also fluctuate due to small-scale irregularities in the ionosphere (Seybold, 2005).

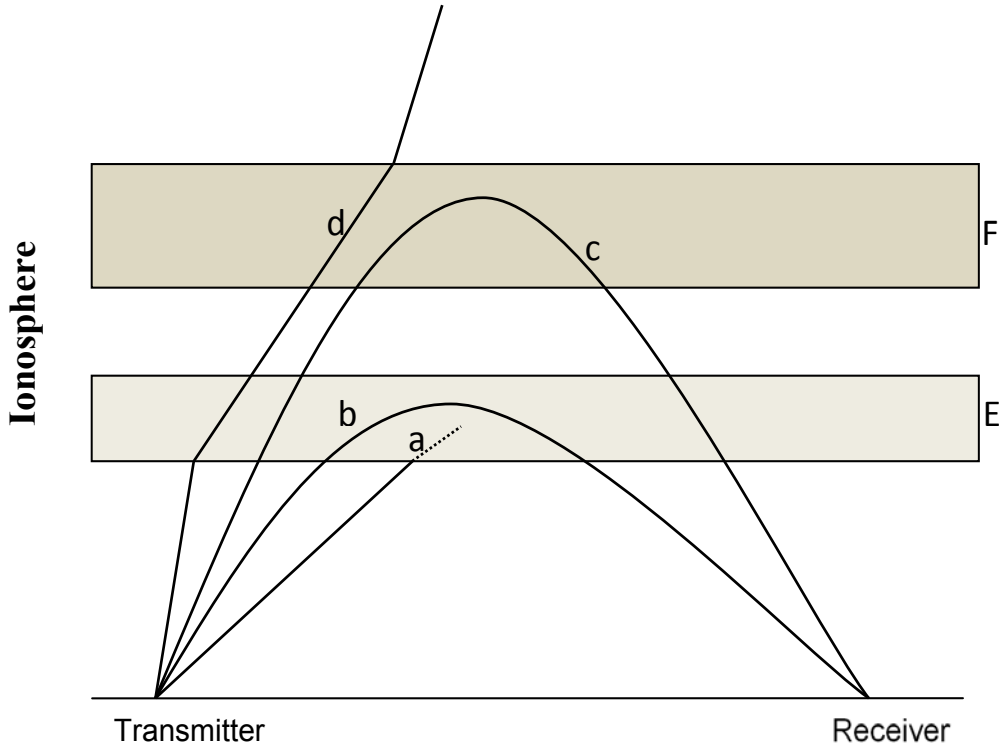

Figure 2.5: Schematic illustration of the propagation of an electromagnetic wave in the ionosphere. Adapted from Sizun (2005).

As shown in figure 2.5, the D layer will absorb the radio wave if the frequency is too low as shown with ray (a). When the frequency increases, the radio wave is refracted and reflected by the E and F layers which allows communication between a transmitter and a receiver (rays b and c). However, if the frequency is too high, the radio wave is refracted but not to the degree required for reflection, as in ray d. In this case the wave disappears in the interplanetary medium instead of being reflected back to the ground. Very high frequencies are important for radio communication between the Earth and satellites. This illustration thus introduces two terms, namely Lowest Usable Frequency (LUF) and the Maximum Usable Frequency (MUF) (Sizun, 2005). For a frequency to be usable, it should be such that LUF $<$ f $<$ MUF. It is important to note that there is no fixed usable frequency for radio communication. The usable frequency is dependent on factors such as the electron density of the medium, the hour of the day, the season and solar activity.

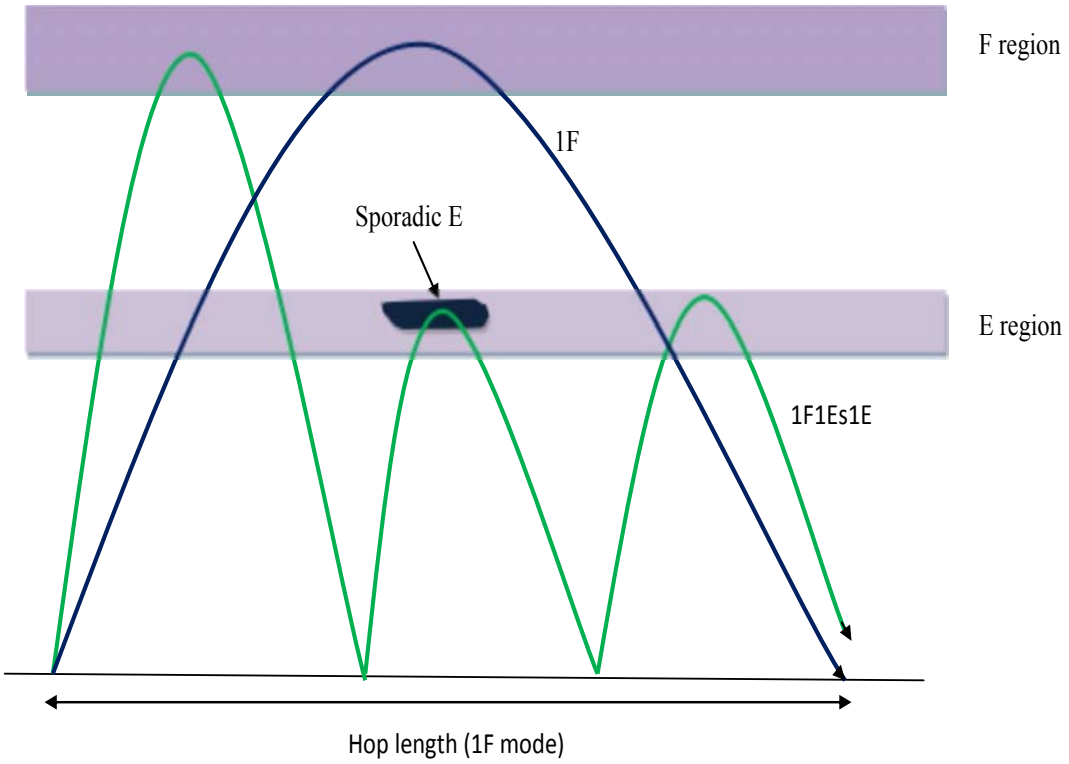

Figure 2.6: Examples of simple and complex propagation modes

Figure 2.6 illustrates simple and complex propagation modes and the hop length. The ground distance covered by a radio signal after reflection by the ionosphere is referred to as the hop length. It depends on the ionospheric height and the Earth's curvature. Multiple hops are required for radio signals travelling greater distances. A sky wave may travel from a transmitter to a receiver via a number of paths such as the first order mode which requires the least number of hops, the second order which requires one extra hop and the n^{th} order which requires $n-1$ extra hops. Simple modes involve reflection by one region (e.g. 1F) and complicated modes involve reflections by two or more regions (e.g. 1F1Es1E). Figure 2.6 shows an example of each mode.

2.4.2 Effect of space weather on HF propagation

HF propagation depends on the ionosphere, but also has to bear with effects which include absorption, refraction, Faraday rotation and scintillation. The choice of a suitable usable frequency is dependent on the ability to predict the conditions of

the ionosphere (Daglis, 2004). Space weather is one of the substantial contributors to ionospheric effects and is a result of the sun's behaviour (mainly solar eruptive events such as solar flares and Coronal Mass Ejections (CMEs)), the nature of Earth's atmosphere and magnetic field and our location in the solar system. It provides a description of the conditions in space that affect the Earth and its technological systems (Goodman, 2005). Severe space weather poses a risk to modern technology including space instruments such as Global Navigation Satellite Systems (GNSS).

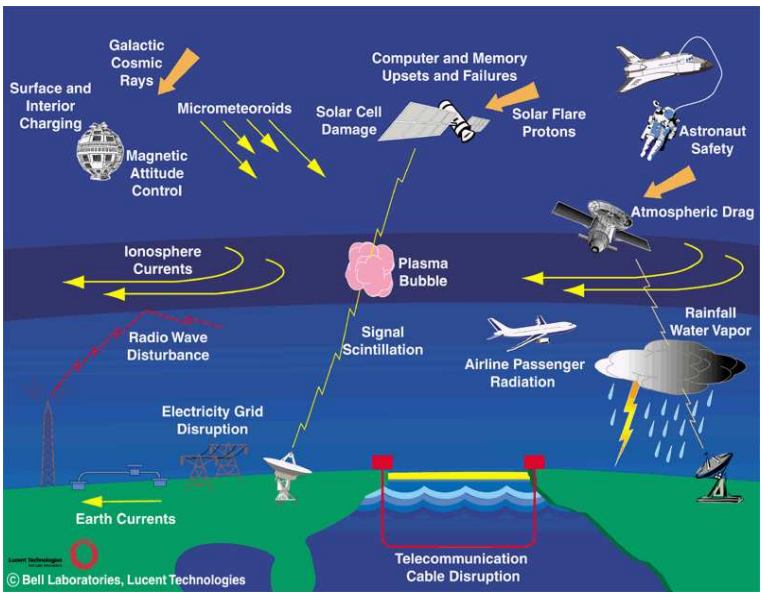

Figure 2.7: Space weather effects on technological systems. Figure obtained from http://www.space.noa.gr/daglis/activities/asi2000,html.

Figure 2.7 shows some of the effects of space weather on technological systems. Radio communication which depends on the ionosphere is affected by space weather. Changes in electron density and ionospheric irregularities as a consequence of adverse space weather may lead to signal degradation or radio blackout. Power systems are often severely affected by geomagnetic storms due to the currents induced by a changing magnetic field. Passengers aboard commercial jets travelling at high altitudes, astronauts and satellite operations are vulnerable to strong radiation (Wernik, 2005). As human dependence on space weather-affected instruments and related technology increases we become more vulnerable to the next approaching peak of solar activity. This raises the urgency to improve on

the accuracy of space weather prediction in order to mitigate the negative effects and risks associated with space weather. It is also urgent that clear information be provided to those who may be affected. This information can be disseminated through research and community awareness programmes (Williamson *et al.*, 2010). Thus prediction models have been developed for space weather forecasting.

2.5 Summary

The Earth's atmosphere was discussed with emphasis on the ionosphere which forms the basis for HF propagation over long distances. Sky wave propagation was presented and shown to be vulnerable to the dynamics of the atmosphere.

Chapter 3

Instrumentation and analysis techniques

3.1 Introduction

This chapter contains a brief description of the instruments used for this project: the HF Doppler radar, ionosonde, Global Positioning System (GPS) receiver, GPS ionospheric scintillation total electron content (TEC) monitor (GISTM) and magnetometer. The data analysis techniques are briefly described. All the instruments are located at Hermanus (34.4° S, 19.2° E) and are operated by the South African National Space Agency (SANSA).

3.2 Instrumentation

The effect of the atmosphere (especially the upper atmosphere) on HF propagation is studied mainly by ionospheric sounding techniques. These techniques use a system of synchronised transmitters and receivers to provide data on HF propagation. The ionosphere is studied using vertical radio sounding (bottomside or topside), backscatter, incoherent scatter sounding, riometers, and low frequency and very low frequency receivers (Sizun, 2005). The vertical or oblique bottomside sounding method uses radio systems located on the Earth's surface. The radio signals are transmitted at various frequencies and the reflected echo is received after a time delay. The virtual reflection height is determined by the delay which corresponds to the radio wave propagation time (Sizun, 2005).

3.2.1 HF Doppler radar

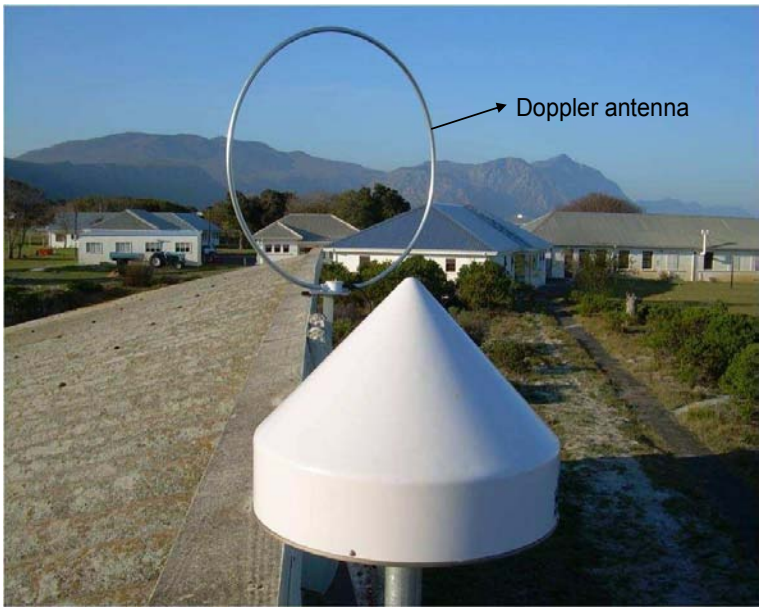

Figure 3.1: HF Doppler radar antenna.

The receiver of the Hermanus HF Doppler radar is based in Hermanus (see figure 3.1) and has transmitters in Cape Town, Worcester and Arniston. This radar uses the Doppler technique as a basis for its measurements. The Doppler technique measures a shift in frequency (Δf) between the transmitted and received signals after total reflection by the ionosphere. Its high time resolution, sensitivity to small frequency changes and capability to do long continuous observations makes it a unique instrument for the study of the atmosphere (Chum *et al.*, 2008).

The principle of Doppler sounding

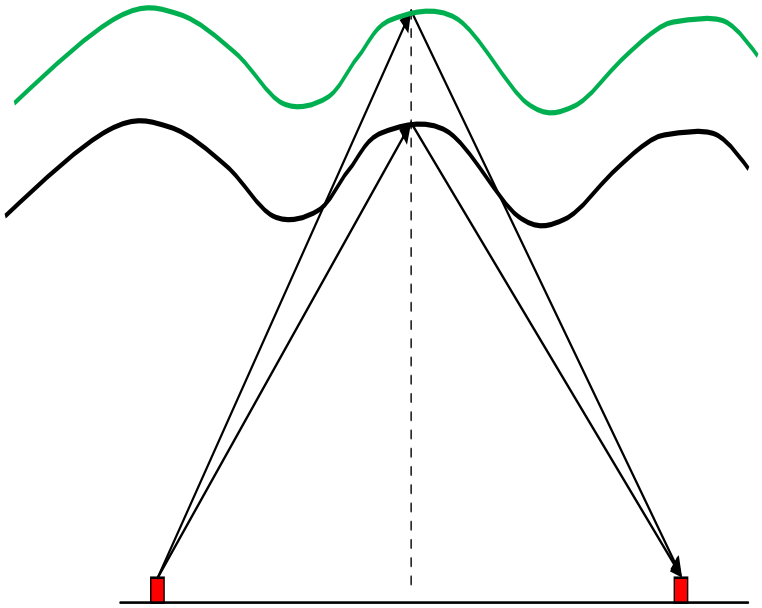

Figure 3.2: A diagrammatical representation of the radar principle.

Figure 3.2 illustrates the reflection of a transmitted signal by a moving layer. Owing to the movement of the reflection layer, the frequency of the received wave is slightly different from the transmitted frequency, a phenomenon known as the Doppler effect. The change in frequency is referred to as the Doppler shift. The Doppler shift in frequency is proportional to the rate at which the phase path length of the signal in the ionosphere changes. The total reflection is a consequence of the refraction of radio waves by ionospheric plasma density gradients. Total reflection at vertical incidence occurs to waves of frequencies lower than the critical frequency of a particular layer of interest in the ionosphere. The shift in frequency between the received and transmitted signals, Δf, is given by

$$\Delta f = \frac{-f}{c}\frac{dP}{dt}, \tag{3.1}$$

where c is the speed of light, f is the sounding frequency and the phase path length, P. The latter is defined as

$$P = \int_z n ds \tag{3.2}$$

The above integration is calculated along the ray path. n is the refractive index for electromagnetic waves.
The sky wave is transmitted and received by a transmitter and receiver located at the earth's surface. This implies that the radio signal travels the distance between the earth's surface and the reflection layer twice, in which case P is given by

$$P = 2\int_0^H n dz \tag{3.3}$$

where z is the height measured from the surface of the earth, and H is the reflection height. Recall from chapter 2 that the simplified form of the Appleton Hartree equation gives the refractive index as

$$n^2 = 1 - \frac{f_p^2}{f^2} = 1 - \frac{e^2 N}{4\pi^2 \epsilon_0 m_e f^2} \tag{3.4}$$

where f_p is the plasma frequency, e is the electron charge, ϵ_0 is the permittivity within a vacuum and m_e is the mass of an electron. It follows from equations 3.1 and 3.3, assuming that for reflection to occur, $z = H, n = 0$, that

$$\Delta f = -2.\frac{f}{c}\frac{d}{dt}\left(\int_0^H n.dz\right) = -2.\frac{f}{c}\int_0^H \frac{\partial n}{\partial N_e}.\frac{\partial N_e}{\partial t}.dz \tag{3.5}$$

where N_e is the electron density. In most cases, the rate of change of the refractive index is neglected and the Doppler shift is regarded as a change in the reflection layer at a velocity $v = \frac{dH}{dt}$. Using this assumption, the calculation of Doppler shift is simplified (Jacobs and Watanabe, 1966; Chum *et al.*, 2010) to be

$$\Delta f = -2f\frac{v}{c} \tag{3.6}$$

Using the equation of continuity, the term $\frac{\partial N_e}{\partial t}$ in the integral in equation 3.5 can be written as

$$-\frac{\partial N_e}{\partial t} = \bigtriangledown.(N_e u) = \bigtriangledown N_e.u + N_e(\bigtriangledown.u) \tag{3.7}$$

where u is the mean velocity of the particles. Performing the first derivative, $\frac{\partial n}{\partial N}$ (from equation 3.4) and substituting into 3.5 it follows that

$$\Delta f = \frac{1}{4\pi^2 \epsilon_0 m_e c f}\int_0^H \frac{1}{n}.\frac{\partial N_e}{\partial t}.dz \tag{3.8}$$

It is clear from equation 3.8 that the Doppler shift, which is a consequence of the change in the signal phase path, depends on the electron density profile of the ionosphere. This is due to the dependence of the refractive index n on the electron density N_e seen in equation 3.4. In a region where $f_p \simeq f$ (equation 3.4), the term $\frac{1}{n}$ in equation 3.8 makes the largest contribution to the Doppler shift. Hence, the highest Doppler shifts are usually observed when the radio waves reflect near the maximum of an ionospheric layer, close to the F2 layer peak (Chum *et al.*, 2009, 2010).

HF Doppler data processing

In May 2010, a continuous HF Doppler sounder which includes processing software was installed at Hermanus (34.4° S, 19.2° E). The three transmitters are in Cape Town (33.9° S, 18.5° E), Worcester (33.6° S, 19.4° E) and Arniston (34.6° S, 20.2° E). These transmitters are 88.2 km, 95.3 km and 85.9 km from the receiver in Hermanus respectively. By means of Direct Digital Synthesis (DDS), the sounding frequency 3.5945 MHz is derived from the 10 MHz Oven Controlled Crystal Oscillator (OCXO). The required frequency at the receiving site is also tuned by means of DDS, however, to obtain a high signal-to-noise ratio, the received frequency is shifted 80 Hz away from the transmitted frequency. The received signal is converted to lower frequencies and digitised using the precise Sigma Delta analogue-to-digital converter. The frequencies of transmitters are shifted by 4 Hz relative to each other which allows the use of only one receiver and the representation of the three traces on one spectrogram. GPS ensures precise time synchronisation and the data is then transmitted and stored on a PC in the control hut. A call sign lasting for 5 s is transmitted every minute because the transmitted frequency falls within the amateur band. The sampling frequency is 305.1758 Hz. The successive spectra were obtained by shifting a Gaussian window of width ~ 10 s by a time step less than the width of the window in the time domain to achieve high frequency-time resolution of the observed Doppler shift. For more information about HF Doppler data processing, the reader is referred to Chum *et al.* (2008, 2009, 2010).

The HF Doppler radar receiver is co-located with the ionosonde, GPS receiver, GISTM receiver and magnetometer. One of the advantages of this co-location is that the virtual height of reflection of the 3.59 MHz wave can be determined

directly from ionograms and it also allows an event correlation analysis with the other radars.

Figure 3.3 shows the four main observatory sites in South Africa and the three

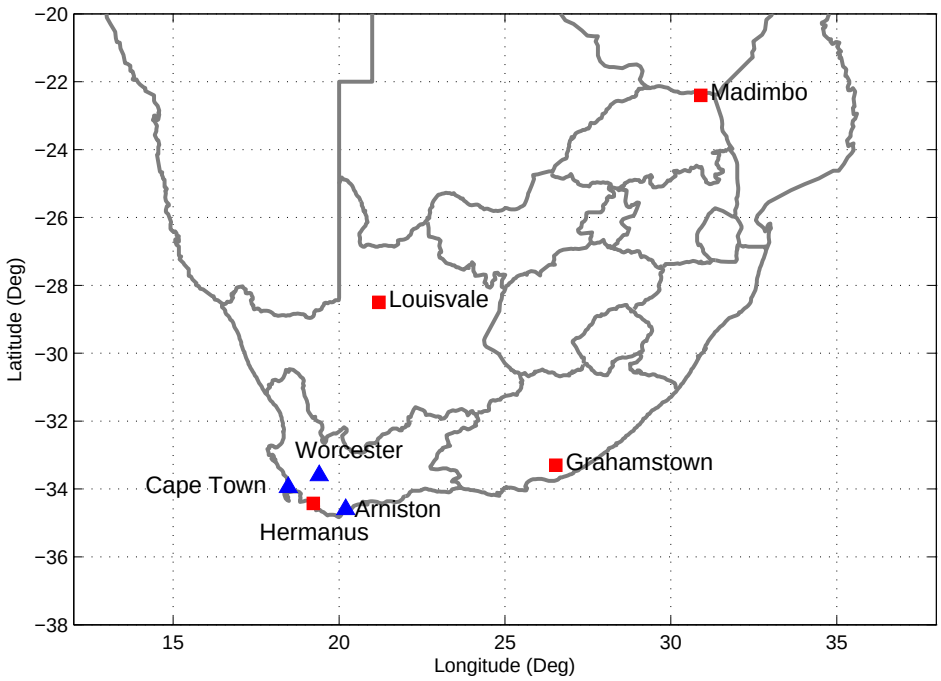

Figure 3.3: Observatory sites in South Africa (red squares) and the three HF Doppler transmitters (blue triangles).

HF Doppler transmitters. Only Hermanus station was chosen for this study since it is the only South African station that hosts co-located radars and instruments. In this study, the correlation analysis was mostly done with a wavelet transform of the weighted average VTEC, GISTM S_4 parameter and the components of the magnetic field.

3.2.2 Ionosonde

An ionosonde is a high frequency radar which sends radio waves vertically into the ionosphere. The frequency can range from below 0.1 MHz to 30 MHz or more (Davies, 1989). Two types of modulation are used by ionosondes, namely the pulse and the chirp modulation methods. The pulse sounders transmit short pulses of

$\sim 100\mu s$ at a high peak power of $1-30$ kW and a frequency sweep range of $1-15$ MHz in a period of $20-60$ seconds. The receiver output of the pulse sounders are peaks in the time domain. The chirp sounders transmit a long pulse of $0.5-1.0$ seconds at a lower peak power of $10-100$ watts and the receiver output are peaks in the frequency domain. In South Africa the pulse modulation method has been standardised for bottomside sounding.

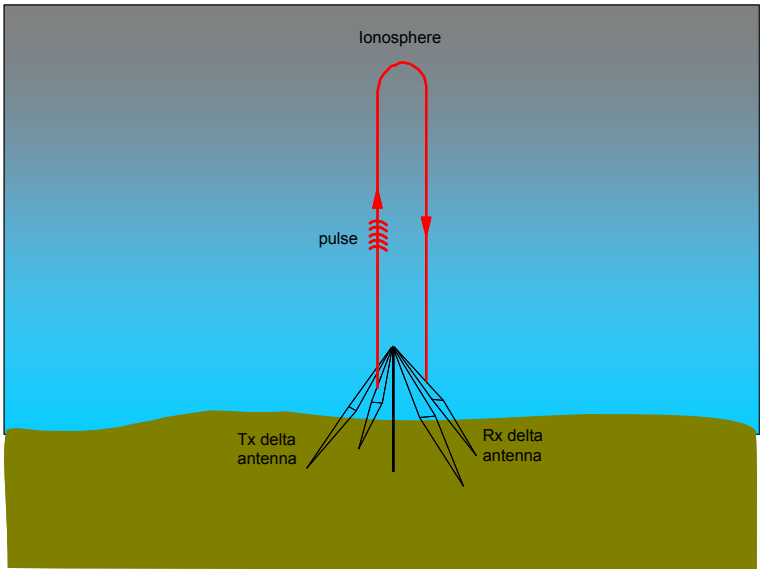

Figure 3.4: A schematic illustration of the standard pulse operation of an ionosonde.

The pulse ionosonde transmits short pulses of radio energy and records the time delay of the reflection of the echo by the ionosphere. The virtual height of reflection (h') is the apparent height of an ionized layer had the wave continued to travel at the speed of light, as determined from the time interval between the transmitted signal and the ionospheric echo at vertical incidence. It is given by

$$h' = \frac{c\tau}{2} = c\int_0^{h_r} \frac{dh}{u} = \int_0^{h_r} \mu' dh \tag{3.9}$$

where c is the speed of light, τ is the echo delay and the factor 2 accounts for the fact that the pulse has to traverse the distance h' twice. u is the group speed and h_r is the real height of reflection (Davies, 1989).
Ionograms are a recording of the variation of the virtual reflection height with frequency. An example is shown in figure 3.5.

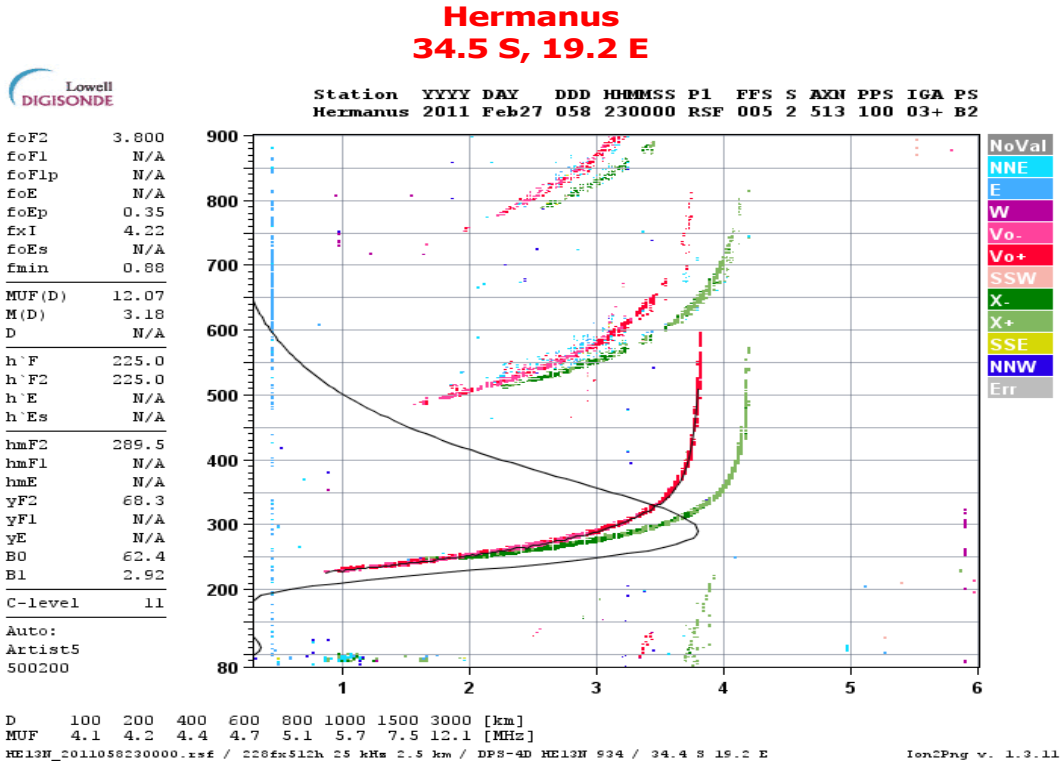

Figure 3.5: An example of an ionogram recorded at Hermanus (34.4° S, 19.2° E) at 23h00 UT.

The presence of the earth's magnetic field makes the ionosphere a doubly refracting medium for radio wave propagation. This explains the two traces on the ionogram. The red and green traces represent the ordinary (O) wave and the extraordinary (X) wave respectively. The vertical assymptotes for these traces represent the critical frequencies foF2 for the O-wave and fxF2 for the X-wave (McNamara, 1990).

(a) (b)

Figure 3.6: (a) Transmitter antenna and (b) Receiver antenna of the Hermanus ionosonde

Figure 3.6 shows the transmitter and receiver antennas for the Hermanus ionosonde. This ionosonde generates electron density profiles for ionograms recorded at intervals of 15 minutes. The generated profile is shown overlaid on the ionogram in figure 3.5 as the smooth black curve. For this study the Standard Archiving Output (SAO)-Explorer software was used for the extraction of the critical frequencies and the true and virtual heights of the reflection layer, as well as for viewing the ionograms. SAO-Explorer is a data analysis tool used for manually verifying, editing, viewing autoscaled ionograms and derived ionospheric characteristics (Reinisch *et al.*, 2004). The derived ionospheric characteristics such as critical frequencies and the heights on the ionogram are automatically scaled by the Automatic Real Time Ionospheric Scaling Technique (ARTIST) software (Reinisch *et al.*, 2004).

3.2.3 Global Positioning System

GPS is a worldwide, satellite-based radio navigation system operated by the United States (US) Department of Defence (DoD). The initial goal for its development was to continuously and accurately determine the position, velocity and time for the US military forces at any location on or near the earth. Civilians were later permitted to use the GPS network and since then it is being used in various fields, including research (Hofmann-Wellenhof *et al.*, 1992). The GPS network consists of mainly three segments, namely space, control and user segments. The GPS

space segment consists of a constellation of 24 satellites which orbit the earth at an inclination of 55° relative to the equator and at a radius of 20 200 km. At any given time and location, at least four satellites are visible to an observer. The satellite vehicles (SVs) orbit the earth in six 11 hour 58 minute orbital planes with 4 satellites in each orbit. Important system parameters are determined when coded radio signals emitted by SVs are decoded by a GPS receiver (Farell and Barth, 1998). The control segment consists of a system of monitor and master control stations and ground antennas. The master control station mainly monitors, maintains and manages the space segment and provides a regular update of the satellite-transmitted navigation messages. The monitor station tracks and gathers ranging data from all the visible GPS satellites (NAVSTARGPS, 1996). The user segment is made up of antennas and receivers which provide positioning, velocity and precise timing information to the user by measuring and decoding radio signals transmitted by the satellites. The design and function of the GPS receivers depend on the requirements of the user (NAVSTARGPS, 1996; Farell and Barth, 1998). GPS satellites transmit radio signals at two frequencies, L1 (1575.42 MHz) and L2 (1227.60 MHz). Two different ranging codes namely coarse/acquisition code (C/A-code) which is modulated on L1 and precision code (P-code) which is modulated on both L1 and L2, are employed in the transmission of GPS signals. The satellite-user range can be determined using these codes, though in most cases the P-code is encrypted and thus requires authorisation (NAVSTARGPS, 1996; Hofmann-Wellenhof *et al.*, 1992).

The GPS signals are greatly affected by the ionosphere as they traverse ionospheric layers and the magnitude of this effect is measured by the total electron content (TEC) and by the frequency of radio waves (Gao and Liu, 2002). TEC is obtained from GPS measurements and is expressed mathematically as

$$TEC = \int_{path} N_e(s)ds \tag{3.10}$$

where $Ne(s)$ is the electron density along the ray path. TEC is defined as the number of electrons per unit square metre along a ray path between a GPS satellite and a receiver and is usually given in total electron content units, TECU (1 TECU = 1×10^{16} electrons/m^2). Two parameters can be derived from observables, namely vertical TEC (VTEC) and slant TEC (STEC). The STEC is the

TEC along the line of sight and the VTEC is derived from the STEC using algorithms such as Adjusted Spherical Harmonic Analysis, ASHA (Opperman *et al.*, 2007). TEC is a good measure of the changes in the structure of the ionospheric electron density as they occur geographically, diurnally and seasonally.
GPS measurements are made using single or dual frequency GPS receivers. However, dual frequency GPS receivers are preferred in TEC computations owing to the fact that they are designed to remove ionospheric errors. A dual frequency GPS receiver comprises of code and carrier phase observations on L1 and L2 frequencies. These observations can be expressed mathematically (Gao and Liu, 2002) as

$$P_1 = \rho + c(dt - dT) + d_{orb} + d_{trop} + k_2 I + b_{P_1} - B_{P_1} + \varepsilon(P_1) \tag{3.11}$$

$$P_2 = \rho + c(dt - dT) + d_{orb} + d_{trop} + k_1 I + b_{P_2} - B_{P_2} + \varepsilon(P_2) \tag{3.12}$$

$$\Phi_1 = \rho + c(dt - dT) + \lambda_1 N_1 + d_{orb} + d_{trop} - k_2 I + b_{\Phi_1} - B_{\Phi_1} + \varepsilon(\Phi_1) \tag{3.13}$$

$$\Phi_2 = \rho + c(dt - dT) + \lambda_2 N_2 + d_{orb} + d_{trop} - k_1 I + b_{\Phi_2} - B_{\Phi_2} + \varepsilon(\Phi_2) \tag{3.14}$$

where
$k_i = f_i^2/(f_1^2 - f_2^2), i = 1, 2,$
P_i and Φ_i are code and carrier phase observations on L_i
ρ is the true geometric range between the receiver and the satellite (m),
c is the speed of light (ms^{-1}),
dt is the satellite clock error with respect to GPS time (s),
dT is the receiver clock error with respect to GPS time (s),
λ_i is the wavelength of the GPS signal on L_i (m),
N_i is the carrier phase integer ambiguity,
d_{trop} is the tropospheric delay (m),
I is the ionospheric delay parameter (m),
d_{orb} is the satellite orbit error (m),
b and B are the satellite and the receiver hardware delays (m) respectively and
$\varepsilon(\Phi_i)$ and $\varepsilon(P_i)$ are the pseudorange and carrier phase measurement noises, including errors due to multipath effects (m).
The linear combination of the pseudorange and carrier phase observations at the

two frequencies are given by

$$\begin{aligned} P_4 &= P_2 - P_1 \\ \Phi_4 &= \Phi_2 - \Phi_1 \end{aligned} \tag{3.15}$$

Substituting equations 3.11 to 3.14 into equations 3.15 gives

$$\begin{aligned} P_4 &= dI + b_p - B_p + \varepsilon(P_2) - \varepsilon(P_1) \\ \Phi_4 &= dI + \lambda N + b_\Phi - B_\Phi + \varepsilon(\Phi_2) - \varepsilon(\Phi_1) \end{aligned} \tag{3.16}$$

where $dI = I(k_1 - k_2)$ is the ionospheric delay,
$b_p = b_{P_2} - b_{P_1}$ and $b_\Phi = b_{\Phi_2} - b_{\Phi_1}$ are the differential satellite delays,
$B_p = B_{P_2} - B_{P_1}$ and $B_\Phi = B_{\Phi_2} - B_{\Phi_1}$ are the differential receiver delays for pseudorange and carrier phase observations respectively,
$\lambda N = \lambda_2 N_2 - \lambda_1 N_1$.
TEC can be related to P_4 and Φ_4 (Schaer, 1999) by

$$P_4 = \left(\frac{1}{f_2^2} - \frac{1}{f_1^2}\right).\alpha.TEC_P \tag{3.17}$$

and

$$\Phi_4 = \left(\frac{1}{f_2^2} - \frac{1}{f_1^2}\right).\alpha.TEC_\Phi \tag{3.18}$$

where $\alpha = 40.3 \times 10^{16}$, TEC_P and TEC_Φ are TEC derived from pseudorange and carrier phase observations respectively. It is important to note that TEC_Φ has less noise compared to TEC_P (Opperman *et al.*, 2007).

Figure 3.7: The GPS antenna for the receiver located in Hermanus (34.4° S, 19.2° E).

Figure 3.7 shows the Hermanus dual frequency GPS receiver antenna. The data from this GPS receiver is recorded in compressed Receiver Independent Exchange (RINEX) format. The RINEX GPS observation data is processed and a MATLAB file consisting of observables such as the PTEC, LTEC and the GPS time is generated. PTEC and LTEC refer to the STEC derived from pseudorange and carrier phase observations respectively.

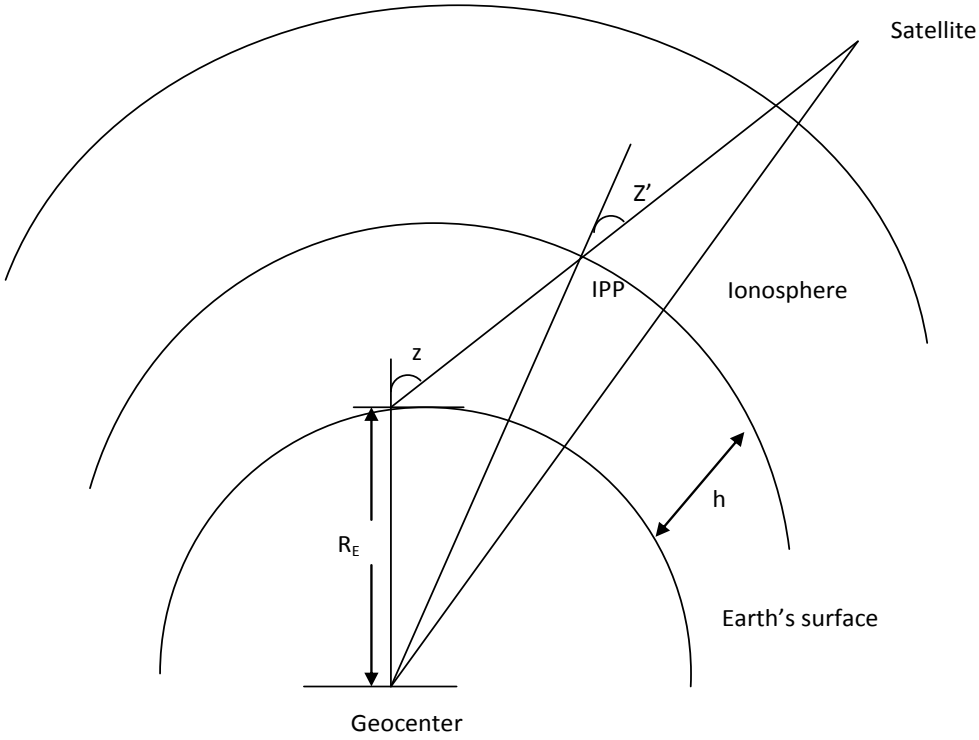

Figure 3.8: Illustration of the GPS signal path. Adopted from Hofmann-Wellenhof *et al.* (1992)

Using the single layer model (SLM), the VTEC is derived from the GPS-derived STEC values by applying the mapping function (Hofmann-Wellenhof *et al.*, 1992; Schaer, 1999; Opperman *et al.*, 2007),

$$sinz' = \frac{R_E}{R_E + h} sinz \tag{3.19}$$

where z is the satellite zenith angle, R_E is the Earth equatorial radius (6378.134 km), h is assumed SLM height (350 km) (see figure 3.8). The VTEC used in this work was derived using ASHA function which models TEC as a spherical harmonic expansion (Opperman *et al.*, 2007)

$$TEC(\lambda, \phi) = \sum_{n=0}^{N} \sum_{m=0}^{n} \bar{P}_{nm}[cos(\phi)] a_{nm} sin(m\lambda) + b_{nm} cos(m\lambda) \tag{3.20}$$

where λ is the ionospheric pierce points (IPP) sun-fixed longitude, ϕ is the IPP co-latitude, $\bar{P}_{nm}$ are the normalised associated Legendre functions, a_{nm} and b_{nm}

are the desired SHM coefficients and n, m are degree and order of SHM expansion. Details of the VTEC derivation using ASHA function were discussed by (Opperman, 2007). A weighted average VTEC at an interval of 1 second was computed as

$$\langle VTEC \rangle = \frac{1}{N} \sum_{1}^{N} (w_i . VTEC_i) \tag{3.21}$$

where N is the number of satellites visible at t_s (each second on a given day), i = 1,2,3,... are individual satellites that are visible at t_s and w_i is the weighting function at t_s given by

$$w_i = \left(\frac{N}{\sum_1^N sin\alpha_i} \right) sin\alpha_i \tag{3.22}$$

α_i are the elevation angles for the satellites visible at t_s. Only observations at elevation angles $\geq 20^\circ$ were considered to minimise multipath errors. The $\langle VTEC \rangle$ values for a period of interest were transformed into a wavelet to observe ionospheric events.

3.2.4 GISTM

The received radio signal is often affected by fluctuations in phase and amplitude, owing to large-scale gradients and small-scale irregularities in the electron concentration, a phenomenon known as scintillation. The GPS ionospheric scintillation total electron content (TEC) monitor (GISTM) network can provide information about the nature of the scintillation activity.

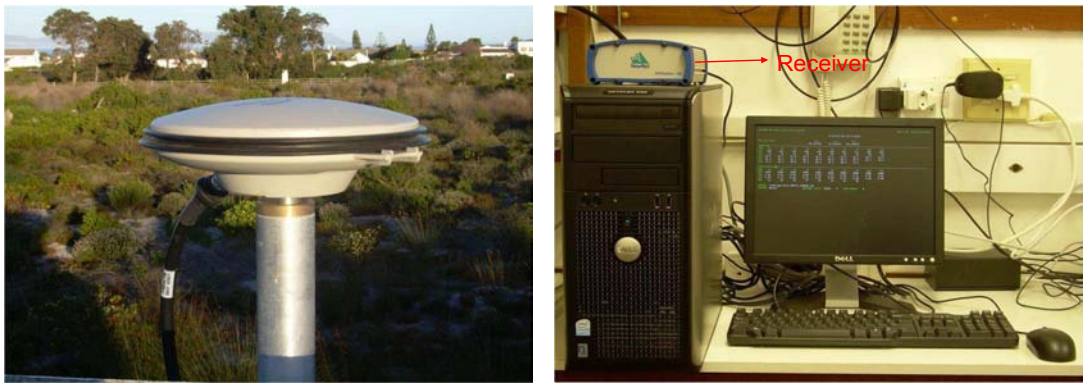

(a) (b)

Figure 3.9: (a) The GISTM antenna and (b) receiver and PC in the control hut at Hermanus.

Figure 3.9 shows the GSV 4004B GISTM antenna and a NovAtel Euro-3M dual frequency receiver located at Hermanus. The main component of the GISTM receiver is a GPS signal monitor which is designed to track and measure amplitude and phase scintillation from the L1 frequency GPS signals and ionospheric TEC from the L1 and L2 frequency GPS signals. The GISTM is capable of monitoring 11 observable GPS satellites simultaneously (GPSSiliconValley, 2004). This GISTM compares phase measurements with actual carrier phase GPS observations using wide bandwidth tracking loops and an internal phase stable ovenised crystal oscillator (Aquino *et al.*, 2004).
This study uses the S_4 index which is a measure of the amplitude scintillation and is defined as the normalised standard deviation of the strength of the received signal, S mathematically expressed as

$$S_4^2 = \frac{\langle S^2 \rangle - \langle S \rangle^2}{\langle S \rangle^2} \tag{3.23}$$

In practice, the angle brackets $\langle\rangle$ are simply time averages of S (Beach and Kintner, 2009). The GISTM software can perform automatic computation of the amplitude scintillation, S_4, and phase scintillation index, σ_ϕ, and their logs over 1, 3, 10 and 60 seconds (GPSSiliconValley, 2004). These computations should be such that only the effects of ionospheric irregularities on radio signals are included. A S_4 index calculated with or without ambient noise can be determined (Beach and Kintner, 2009). In this study, the corrected S_4 index calculated by excluding the effects of noise over 60 seconds was used.

3.2.5 Magnetometer

Hermanus is one of the four permanent geomagnetic observatories in Southern Africa operated by the SANSA Space Science. Absolute measurements, made in a single absolute hut, are carried out on a regular basis by means of a DI-flux magnetometer. Figure 3.10 is an illustration of the geomagnetic field components. The DI-flux magnetometer at SANSA Space Science Directorate measures the angles D and I. The total magnetic field intensity, F, was measured by means of

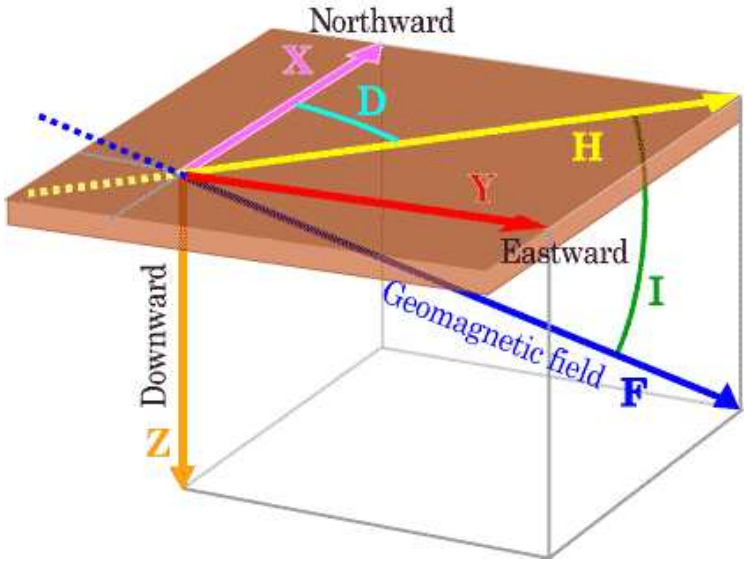

Figure 3.10: Components of the magnetic field.

an Overhauser Magnetometer. The absolute values H and Z are then derived from

$$H = FcosI$$
$$Z = FsinI \tag{3.24}$$

where H, Z and F are field values at the time of the I measurement (Nahayo, 2009). In this study, the D and H magnetic components sampled at 5 seconds for a particular period of interest were analysed for comparison with the Doppler observations.

3.3 Wavelet Analysis

Wavelet analysis is a signal processing technique which refers to the decomposition of a signal into shifted and scaled forms of the original or mother wavelet (Misisti *et al.*, 2009). Scaling and shifting in this case refer to stretching or compression of the wavelet and delaying or hurrying its onset respectively. Wavelet analysis also involves expansion of functions in terms of wavelets which are generated by translating and expanding the mother wavelet. Examples of mother wavelets include Morlet, Meyer, Haar and Daubechies wavelets (Lee and Yamamoto, 1994). Wavelet analysis has the capability to reveal details such as breakdown points

or data gaps and discontinuities that are missed by other techniques (Lee and Yamamoto, 1994). A signal can be compressed or de-noised by wavelet analysis without considerable degradation (Misisti *et al.*, 2009), and the ability to analyse rapidly and sharply changing transcient signals makes this a preferred signal processing technique in various fields including communication, geophysics and other signal processing related research fields (Lee and Yamamoto, 1994; Torrence and Compo, 1998). Wavelet analysis has also proved useful in the analysis of data for this research.

Continuous Wavelet Transform (CWT)

The sum over all time of the signal multiplied by scaled, shifted forms of a wavelet function ψ is referred to as the continuous wavelet transform (CWT).

$$C(scale, position) = \int_{-\infty}^{\infty} f(t)\psi(scale, position, t)dt \tag{3.25}$$

A CWT yields a number of wavelet coefficients C (as functions of scale and position) which when multiplied by a suitable scaled and shifted wavelet gives the wavelets that form the mother signal (Misisti *et al.*, 2009).
A complex-valued function ψ that satisfies the following conditions is assumed

$$\int_{-\infty}^{\infty} |\psi(t)|^2 dt < \infty \tag{3.26}$$

$$c_\psi = 2\pi \int_{-\infty}^{\infty} \frac{|\Psi(\omega)|^2}{\omega} d\omega < \infty \tag{3.27}$$

where the function ψ is the original wavelet and Ψ is the Fourier transform of ψ. The first condition indicates that the function ψ has finite energy and the second condition indicates that $\Psi(0) = 0$ if $\Psi(\omega)$ is smooth. This condition is known as the admissibility condition (Lee and Yamamoto, 1994).
Consider a time series, x_n, with equal time spacing δt and the time index, $n = 0...N-1$. Assume a wavelet function, $\psi_0(\eta)$, (η is a non-dimensional time parameter) which satisfies the conditions described in equations 3.21 and 3.22.
The CWT of this time series is defined as the convolution of x_n with a scaled and

translated form of the wavelet function, $\Psi_0(\eta)$

$$W_n(s) = \sum_{n'=0}^{N-1} x_{n'} \psi^* \left(\frac{(n'-n)\delta t}{s} \right) \tag{3.28}$$

where the complex conjugate is indicated by $(*)$, s is the wavelet scale and N is the number of points in the time series. The dropping of the subscript 0 indicates a normalisation of ψ. The convolution in equation 3.23 should be done N times for each s to approximate the CWT. The convolution theorem allows simultaneous convolutions in Fourier space using a discrete Fourier transform (DFT). The DFT of x_n is given by

$$\hat{x}_k = \frac{1}{N} \sum_{n=0}^{N-1} x_n e^{\frac{-2\pi i k n}{N}} \tag{3.29}$$

where $k = 0...N-1$ is the frequency index. The convolution theorem gives the wavelet transform as the inverse Fourier transform of the product

$$W_n(s) = \sum_{k=0}^{N-1} \hat{x}_k \hat{\psi}^*(s\omega_k) e^{i\omega_k n \delta t} \tag{3.30}$$

where $\hat{\psi}(s\omega)$ is the Fourier transform of $\psi(t/s)$ (in the continuous limit) and the angular frequency is

$$\omega_k = \begin{cases} \frac{2\pi k}{N\delta t} & k \geqslant \frac{N}{2} \\ \frac{-2\pi k}{N\delta t} & k < \frac{N}{2} \end{cases}$$

The CWT for a given s over all n can be computed simultaneously using equation 3.25 and a standard routine for Fourier transform (Torrence and Compo, 1998).

Morlet wavelet

The Fourier transform of the Morlet wavelet is a shifted Gaussian waveform and is adjusted slightly so that $\Psi(0) = 0$ (Lee and Yamamoto, 1994)

$$\Psi(\omega) = e^{\frac{-(\omega-\omega_0)}{2}} - e^{\frac{-\omega^2}{2} - \frac{\omega_0^2}{2}} \tag{3.31}$$

$$\psi t = (e^{-iw_0 t - e^{\frac{\omega^2}{2}}}) e^{\frac{-t^2}{2}} \tag{3.32}$$

In most cases, the choice of ω_0 is such that the ratio of the highest maximum is $\sim \frac{1}{2}$, i.e.,

$$\omega_0 = (\frac{2}{ln2})^{\frac{1}{2}} \simeq 5 \tag{3.33}$$

So, for practical purposes $\omega_0 = 5$. The second term in equation 3.26 becomes too small on substituting for this ω_0 and can therefore be ignored. The Morlet wavelet can be regarded as a Gaussian waveform that is modulated.

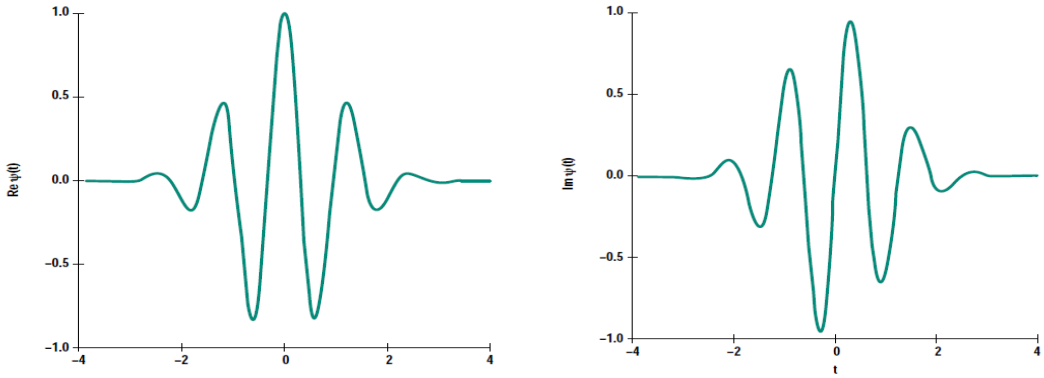

(a) (b)

Figure 3.11: (a) Real part of the Morlet mother wavelet with $\omega_0 = 5$ (b) Imaginary part of the Morlet mother wavelet with $\omega_0 = 5$ (Lee and Yamamoto, 1994)

This provides a complex function with the real and imaginary parts as illustrated in figure 3.11.

3.4 Summary

This chapter discussed the co-located radars and instruments. It described how the data was obtained, as well as wavelet analysis, a signal processing technique used in the data analysis.

Chapter 4

Results

4.1 Introduction

Event periods were analysed for the identification of wave-like structures, Doppler spread, sudden frequency deviation and Doppler oscillations associated with geomagnetic pulsations. Events observed by the Doppler radar were analysed using data from the GPS receiver, GISTIM and ionosonde.

4.2 Wave-like structures

Wave-like structures were identified by manually checking the spectrograms recorded by the Doppler radar. A wavelet analysis of the signal at the identified period was carried out. Similarly, a wavelet analysis of the weighted VTEC and magnetic field components was done for a one-hour period corresponding to the Doppler event, plus or minus 3 hours, to take care of any time delays. Each component of the magnetic field was considered separately and only that which compared well with the Doppler data was included. In the case of VTEC, all the satellites visible during this time range were considered. However, only observations that correlated with the Doppler radar event were included. The S_4 index for the visible satellites in the chosen time range was analysed. Only a few examples are presented. The ionosonde sampling rate is 15 minutes and thus is not suitable for the investigation of ionospheric fluctuations on the time scale of 1 - 30 minutes as mostly observed by the continuous Doppler radar. Continuous Doppler spectrograms (8-hour period) are generated from the HF Doppler radar data. However, for a detailed

display of small changes in the Doppler shift, 1-hour spectrograms were used for this study. Most of the results discussed cover the period from May 27, 2010 to November 2010. Wave-like structures were identified by visual inspection of the detailed spectrograms and the percentage of occurrence computed as

$$P = \frac{N_w}{N_{tot}} \times 100\% \tag{4.1}$$

where P is the percentage of occurrence, N_w is the total number of spectrograms with wave-like structures and N_{tot} is the total number of spectrograms viewed per month or day. Most of the wave-like structures occurred at 15h00, 14h00 and

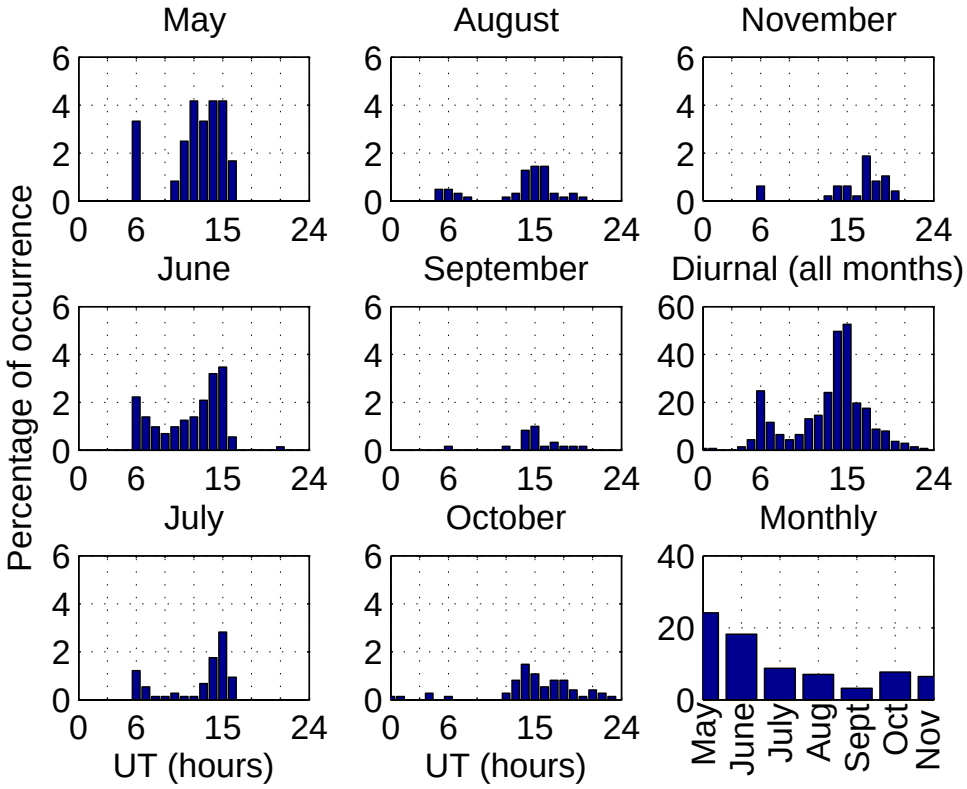

Figure 4.1: Bar graphs showing diurnal and monthly percentage of occurrence of the wave-like structures for the period of May to November 2010.

06h00 UT and in May, June and July as reflected in figure 4.1. This observation could be an indication of diurnal and seasonal variation of this kind of structure, although 7 months is too short a period to make absolute conclusions about such variations. The seasonal variation of the diurnal distribution of the wave-like struc-

tures is evident in figure 4.1, bottom right plot. This is attributed to the change in the sunset and sunrise times across seasons (Šauli *et al.*, 2006). Davies and Baker (1966) attributed the sunset/sunrise dependence of fluctuations of Doppler shift to changes in solar ionising radiation. They also note that frequency fluctuations on a geomagnetically disturbed day are larger and more spread compared to those on a quiet day. During the day, amplitudes of the Doppler shift are higher (more

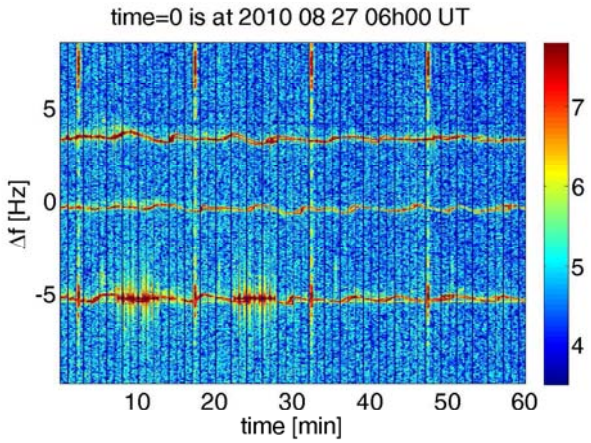

(a)

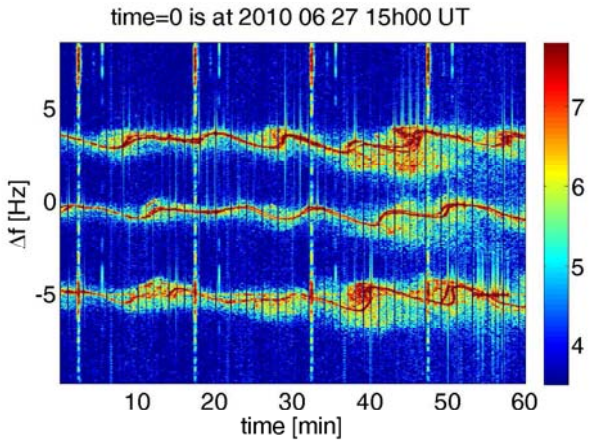

(b)

Figure 4.2: Example of Doppler spectrograms showing a wave-like structure in the (a) morning and (b) evening.

defined) near sunset compared to those near sunrise as shown in figure 4.2. A decrease in the Doppler shift amplitudes was observed across the evaluated months (May to November). The percentage of occurrence also decreases towards the summer months. According to Hines (1960) the presence of travelling ionospheric

disturbances (TIDs), which are wave-like fluctuations of the electron density, are a common feature in the ionospheric F region and a manifestation of the passage of acoustic gravity waves (AGWs) through the neutral atmosphere. Šauli *et al.* (2006) made similar observations and explained the diurnal occurrence in terms of solar ionising radiation and/or gravity waves caused by the passage of the solar terminator. Šauli *et al.* (2006) explained the contribution of solar ionising radiation in terms of an enhancement in ionospheric electron density caused by an increase in photoionisation. The increase in the electron density leads to a decrease in the radio phase path length which manifests as an increase in the Doppler frequency shift. These Doppler frequency fluctuations are associated with changes in the reflection height. They are also attributed to changes in the electron density near the reflection level. On the other hand, the solar terminator is described as a moving border between dayside and nightside of the ionosphere. This border is characterised by strong changes in pressure, temperature and electron concentration in the neutral atmosphere. These changes affect the stability of the plasma in the ionosphere and the process of gaining stability introduces wave activity. In general, the cause of wave-like structures can be attributed to the fast cooling of the atmosphere and changes in the reflection height (Šauli *et al.*, 2006, and references therein). Georges (1968) explains the seasonal variation in terms of mesospheric temperature changes which give rise to more gravity waves and therefore more wave-like structures in the reflected signal. Šindelářová *et al.* (2009) observed and analysed wave activity in the ionosphere with periods from 2 to 30 minutes during tropospheric convective storms. A connection between micropulsations of the geomagnetic field and short period ionospheric oscillations has been studied/described/discussed by several authors (e.g. Sutcliffe and Poole, 1989, 1990; Menk, 1992; Marshall and Menk, 1999; Waters *et al.*, 2007; Chum *et al.*, 2009). Special types of wave-like structures that form S-shaped signature can be observed in Doppler shift spectrograms. The S-shaped signature can be observed if three different rays are simultaneously received on the specific sounding path. Figure 4.3 shows selected examples of S-shaped signatures observed in the Doppler shift spectrograms. The S-shapes vary in shape and size, but the basic S-shape is always evident. Their diurnal and seasonal variation follow the general trend of wave-like structures.

In this study most of the observed S-shapes occurred at sunset. Chum *et al.* (2010)

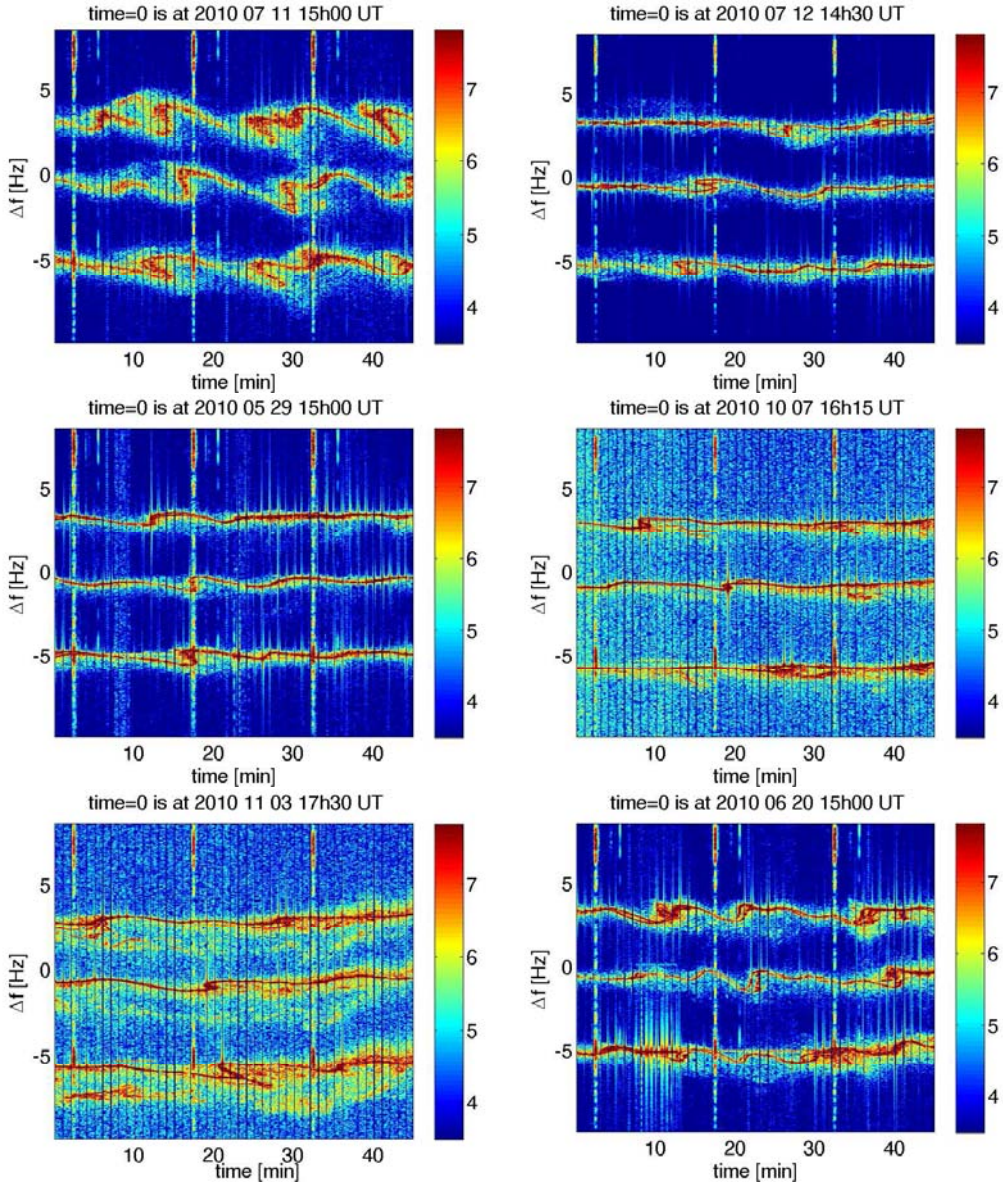

Figure 4.3: Examples of Doppler shift spectrograms displaying S-shapes on the three different sounding paths.

similarly observed most S-shapes at sunset or sunrise. The reflection height of all the S-shaped structures, estimated by using the ionosonde co-located with the HF Doppler radar in Hermanus, was between $\sim$ 180 and 300 km. This could imply that the existance of these structures is due to reflection from the F layer.
A necessary condition to observe the S-shaped signature is that the radius of curvature of the disturbance is less than the reflection height (Davies and Baker, 1966).

If the disturbance moves horizontally or quasi-horizontally, let us assume from left to right, then the left echo will have a positive frequency shift, the right echo will have a negative frequency shift, and the center echo will experience an intermediate frequency shift at the same time. The zero Doppler shift of the center echo is observed when the top of the disturbance passes over the midpoint between the transmitter and receiver if the disturbance propagated strictly horizontally. Recently, Chum *et al.* (2010) used the time differences between the observations of corresponding S-shaped signatures on different sounding paths to calculate the horizontal velocities of gravity waves in the ionosphere. The investigation of horizontal propagation of gravity waves in South Africa will be presented in a separate paper.

4.2.1 The 19 October 2010 event

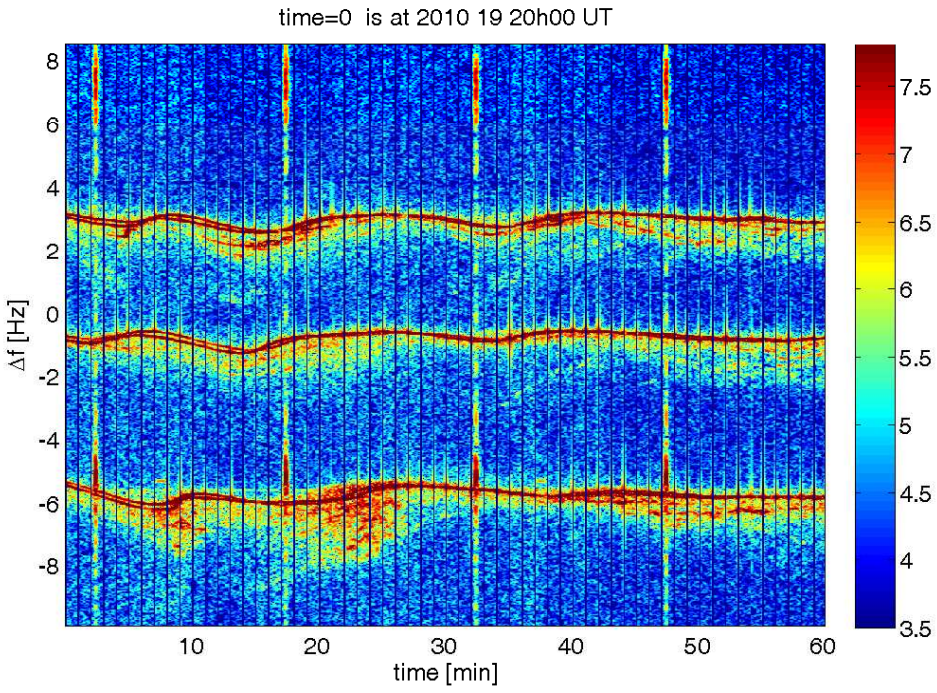

Figure 4.4: Doppler shift spectrogram recorded on 19 October 2010 at 20h00 UT.

Figure 4.4 shows a Doppler shift spectrogram recorded on 19 October 2010 at 20h00 UT. The wave-like structure which was observed between 20h00 and 20h30 UT is not pronounced, because of the monthly trend of the wave amplitude as

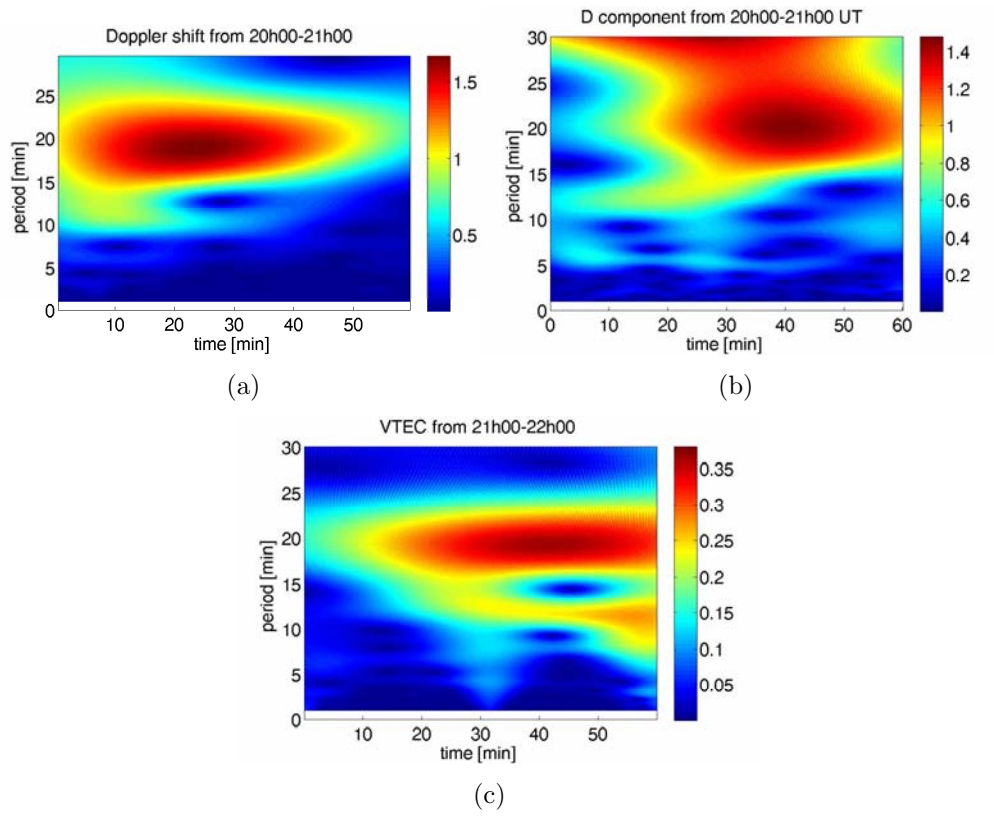

Figure 4.5: Wavelet transform of the (a) Doppler signal (b) D component of the magnetic field (c) VTEC.

explained earlier. This example was included to give a fair representation of the months considered for data analysis.

The Doppler data was compared with the weighted VTEC (see equation 3.21) and the components of the magnetic field measured on the ground in Hermanus. The sampling periods of the VTEC and magnetic field components were 1 s and 5 s respectively. Figure 4.5 shows the wavelet transform (WT) of the Doppler signal, VTEC and the D component of the magnetic field. The WT of these signals show a 20-minute wave. Wave activity was observed between 20h10 - 20h30 UT, 20h30 - 20h50 UT and about an hour later in the Doppler signal, D component of the magnetic field and VTEC respectively. The peak of the wave activity is observed with a time delay in the different signals. The time delay of the 20-minute wave observed by the HF Doppler radar and GPS receiver could be associated with a travelling disturbance which in this case is classified as a medium-scale travelling

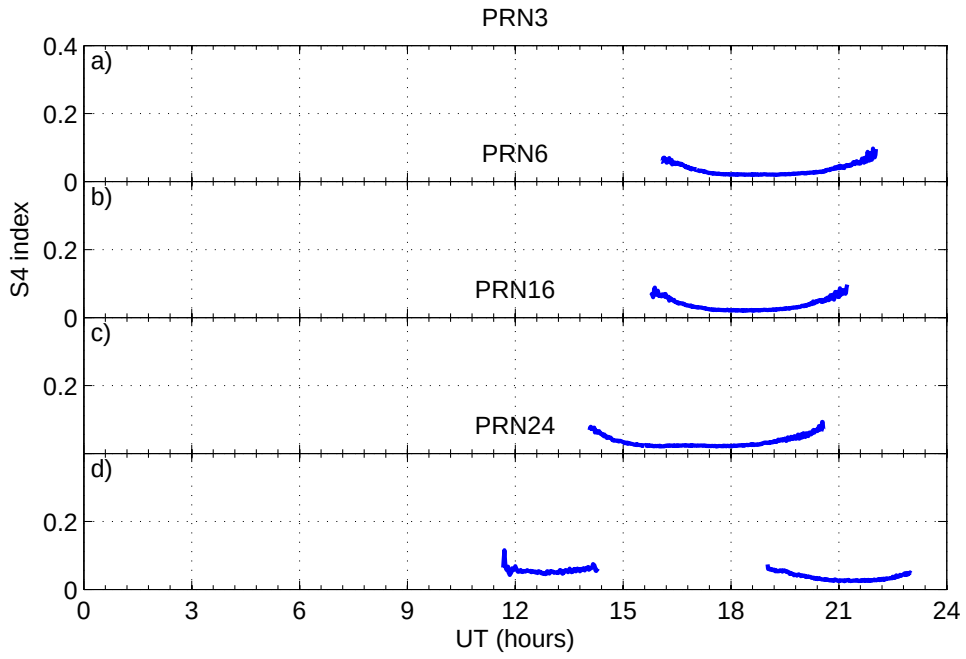

Figure 4.6: Variation of S_4 index on 19 October 2010.

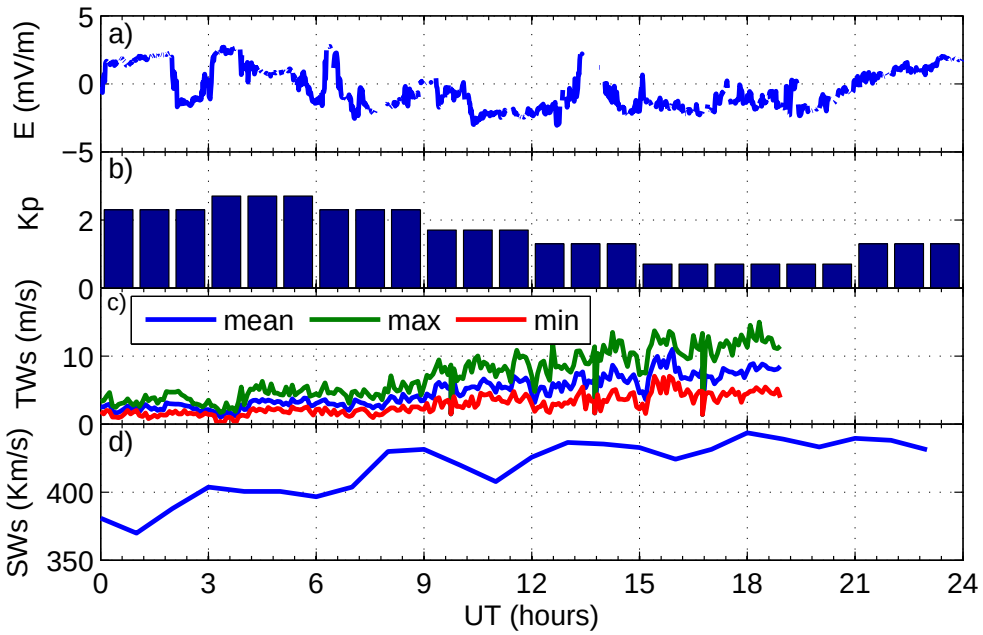

Figure 4.7: Variation of the electric field, Kp index, terrestrial wind speed (TWs) and the solar wind speed (SWs) on 19 October 2010.

ionospheric disturbance (MSTID). TIDs with a wavelength of several hundred kilometers, period of 15 - 60 minutes were classified by Hunsucker (1982) as MSTIDs. Chum *et al.* (2009) observed that the ionospheric oscillations induced by the MHD or ULF waves are usually observed simultaneously and those induced by TIDs have a time delay on all sounding paths. A close look at figure 4.4 shows a time delay (from the lower trace to the upper one) in the wave-like structure between 20h00 and 20h30 UT. The wave observed in the VTEC could be an effect of the ionospheric oscillation on the GPS signals that traverse it.

The HF Doppler radar observations on 19 October 2010 were also compared with the S_4 index. The S_4 index is a measure of ionospheric amplitude scintillation (see equation 3.23). Ionospheric electron density irregularities which are caused by the turbulence of the ionised upper atmosphere are known to scatter radio waves and in the process cause amplitude and phase scintillations. Scintillation events are mostly observed during periods of maximum solar activity when there is an enhancement in the ionisation density (Basua *et al.*, 2002). Ionospheric irregularities are associated with plasma instabilities and are often described as regions of depleted plasma. Mid-latitude scintillations are not a common phenomenon and are associated with magnetic storms and the $E \times B$ instability (Kintner *et al.*, 2007). In order to get a meaningful sample of the scintillation events and for purposes of differentiating between weak, moderate and strong scintillations a threshold of ~ 0.25 for S_4 is always chosen (Spogli *et al.*, 2009).
Figure 4.6 shows the variation of the S_4 index for the satellites PRN3, PRN6, PRN16 and PRN24 on 19 October 2010. Only satellites visible between $\sim$ 18h00 to 22h00 UT were included. The choice of the time range was explained earlier. On all these satellites, the S_4 index was < 0.2, an indication that there were no observed scintillations on this particular day. TIDs are known to create ionospheric irregularities, which in turn cause scintillation in the GPS radio signals. Therefore, absence of a scintillation event corresponding to the event shown in figure 4.4 implies that the MSTID observed by the HF Doppler radar and GPS receiver, as shown in figure 4.5, may not have caused significant scintillations in the GPS radio signals.
This result is representative since similar observations by satellites during the other events showed no scintillations.

Figure 4.7 shows the variation of the electric field, Kp index, terrestrial and solar wind speed on 19 October 2010. The Kp index of < 4 indicates that it was a geomagnetically quiet day. The E-field fluctuated between ~ -3 and ~ 3 mV/m. The average terrestrial wind speed was < 10 m/s. The solar wind during this period was in the range of ~ 380 - 430 km/s.
The electric field (E-field) referred to in this work is a cross product of the interplanetary magnetic field (IMF) B_z and the solar wind velocity. Morton and Mathews (1993) suggested that E-fields $\gtrsim 3$ mV/m are capable of disrupting the mid-latitude layering process. Meteorological activity in the lower atmosphere is known to emit infrasound and gravity waves which may propagate into the upper atmosphere (e.g. Walterscheid and Hickey, 2005; Nasyrov, 2009; Vadas and Fritts, 2004; Sauli and Boska, 2004) and which can manifest themselves as small/medium scale wave-like structures in the Doppler shift spectrograms. The solar wind is known to be a source of ULF waves some of which are carried by and propagate through the solar wind from the sun. An increase in solar wind velocity has an influence on the ULF waves, which are known to induce ionospheric oscillations (Sutcliffe and Poole, 1989, 1990; McPherron, 2005; Chum *et al.*, 2009). Therefore, the observed wave-like structures on 19 October 2010 cannot be associated with geomagnetic sub-/storm activity. Even though the terrestrial wind speed was < 10 m/s, the effect of gravity waves of a different origin cannot be ruled out. The effect of ULF waves of solar wind origin and the changes in the E-fields could have contributed to these structures.

4.2.2 The 5 November 2010 event

Figure 4.8 shows a Doppler shift spectrogram recorded on 5 November 2010 at 20h00 UT. The wave-like structures are more pronounced than in the previous example illustrated in figure 4.4. The WT of the Doppler signal, H component of the magnetic field and VTEC are shown in figure 4.9. Figure 4.9 shows a time delay of the $\sim$ 20-minute wave in the different instruments, which peaks between 20h10 - 20h30 and 20h30 - 20h40 UT for the Doppler signal and the H component of the magnetic field respectively. However, there was no corresponding wave activity in the VTEC. There is a time delay of about 10 minutes between the ionospheric oscillations and the pulsations of the H component of the magnetic

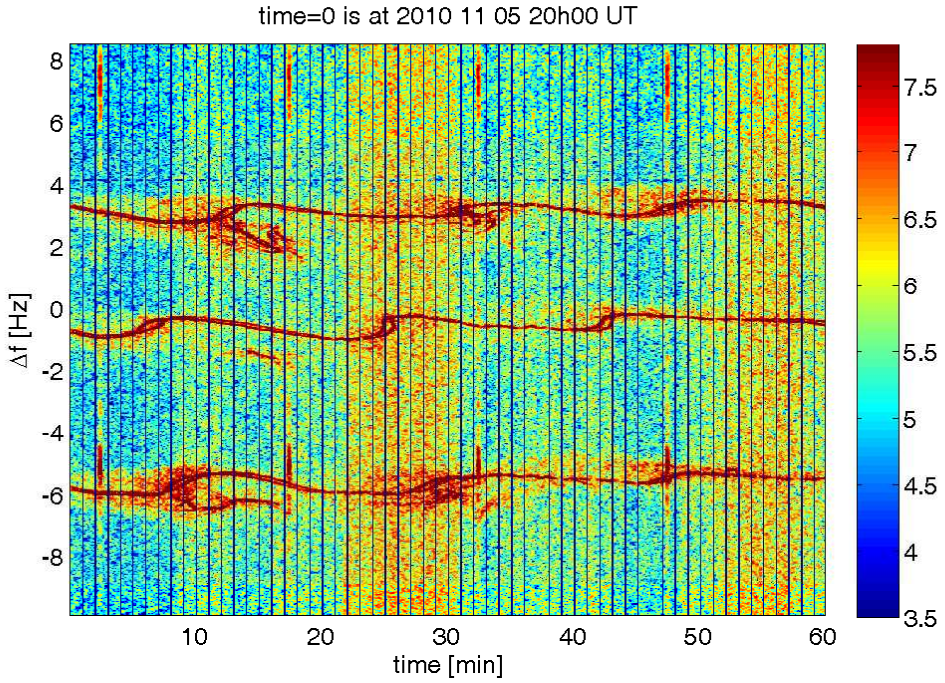

Figure 4.8: Doppler shift spectrogram recorded on 05 November 2010 at 20h00 UT

field. As shown in figure 4.10, 5 November 2010 was a geomagnetically quiet day. The E-field varied between ~ -2 and ~ 2 mV/m, the average wind speed was < 8 m/s and the solar wind increased between 12h00 UT and 21h00 UT from 300 to ~ 380 km/s. Geomagnetic sub-/storms can be discarded as a cause of the wave-like structures. Auroral activity during geomagnetic storms is known to induce large-scale waves in the ionosphere (Šauli *et al.*, 2006, and references therein). The small- and medium-scale waves such as the ones mentioned in this thesis, are much more common than the large-scale waves and are believed to originate from the lower atmosphere and transported to the ionosphere by gravity waves of various origin (Hines, 1960; Hunsucker, 1982; Boska *et al.*, 2003; Šindelářová *et al.*, 2009). The observed waves are probably TIDs or gravity waves, respectively, since they are observed with time delays between different Doppler sounding paths (Chum *et al.*, 2010). The ionospheric oscillations induced by the ULF waves are usually observed simultaneously on all sounding paths (Chum *et al.*, 2009). The average terrestrial wind speed may have been too low to cause a significant effect. The solar wind was constant during the day.

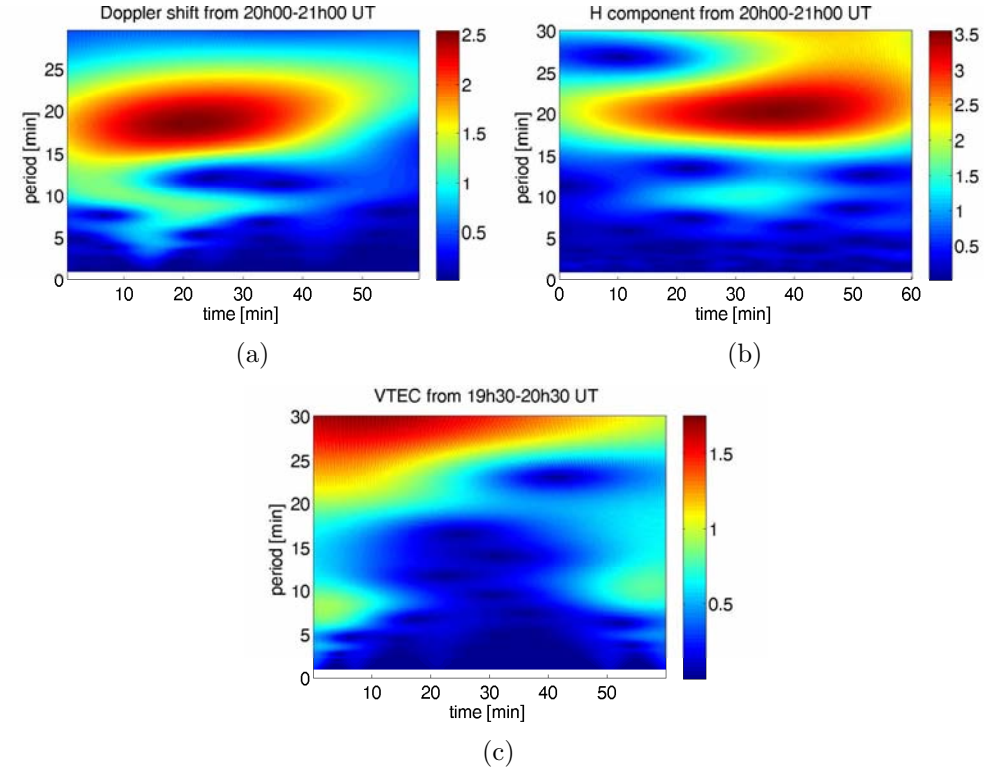

Figure 4.9: WT of the Doppler signal, H component of the magnetic field and VTEC.

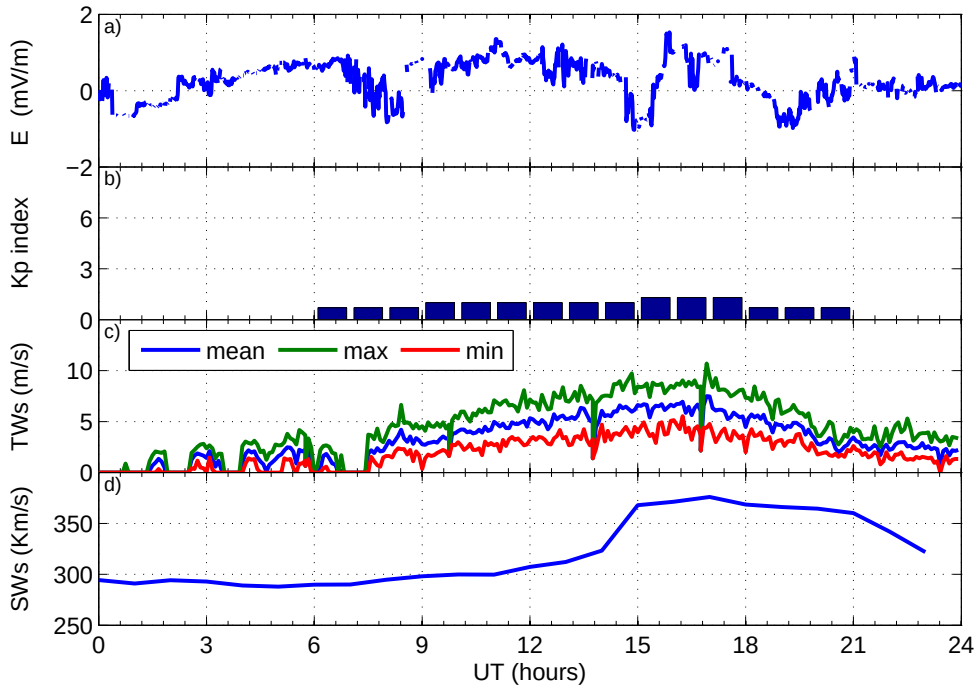

Figure 4.10: Variation of the electric field, Kp index, terrestrial wind and the solar wind on 5 November 2010.

4.2.3 The 29 May 2010 event

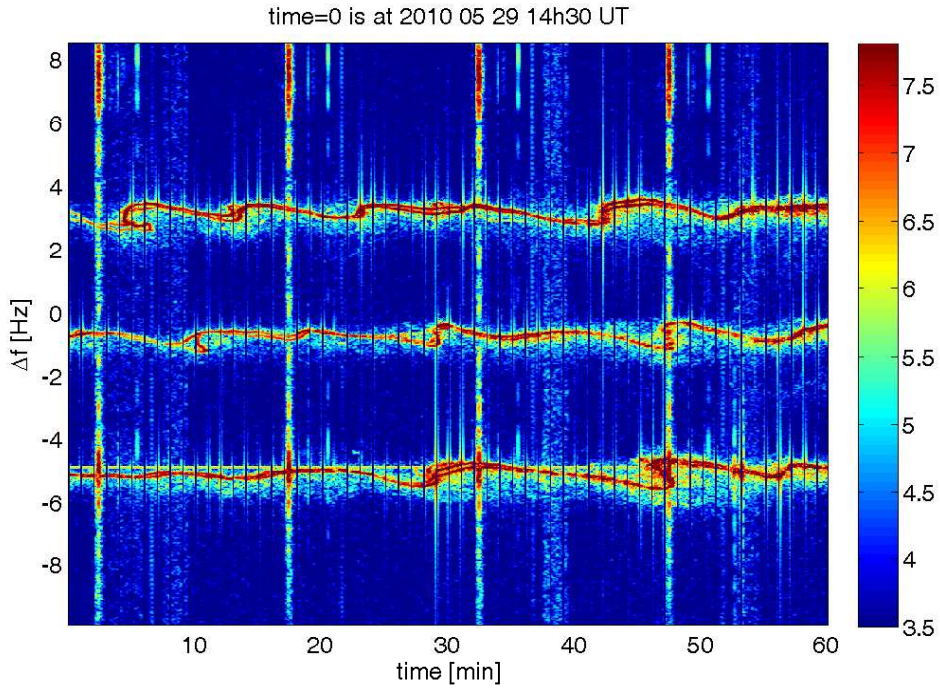

Figure 4.11: Doppler shift spectrogram recorded on 29 May 2010 at 14h30 UT.

Figure 4.2.3 shows the Doppler shift spectrogram recorded on 29 May 2010 at 14h30 UT.

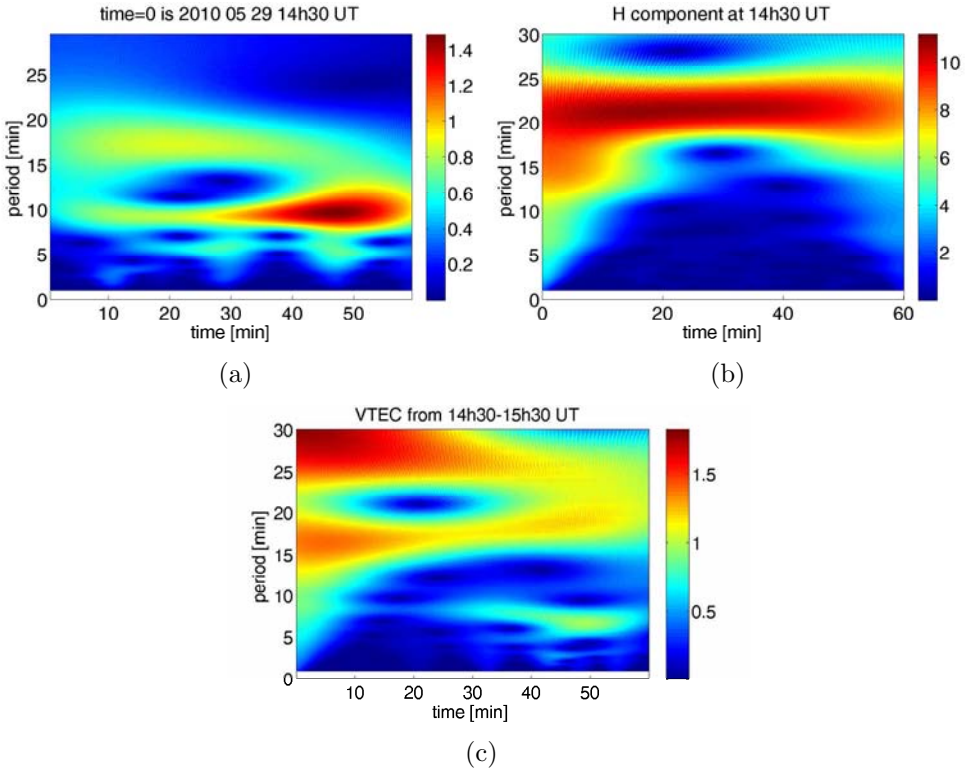

Figure 4.12: WT of the (a) Doppler signal (b) H component of the magnetic field and (c) VTEC.

Figure 4.12 shows WT of the Doppler signal, the H component of the magnetic field and VTEC. The Doppler signal shows a distinct 10-minute wave. The magnetic pulsations of the H component occur throughout the hour with a peak period of about 21 minutes. There is no significant wave activity in VTEC. The 10-minute wave observed in the Doppler signal bears no relationship to the VTEC and magnetic pulsations.

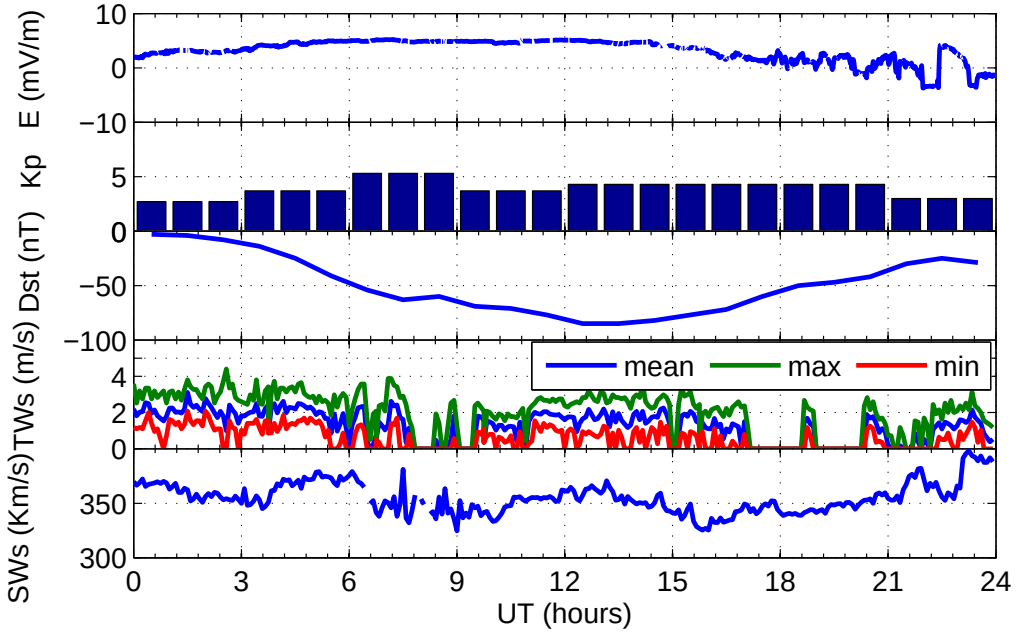

Figure 4.13: Variation of the electric field, Kp index, Dst, terrestrial wind and the solar wind on 29 May 2010.

Figure 4.13 shows the variation of the electric field, Kp index, Dst, terrestrial wind and the solar wind speed on 29 May 2010. There was a geomagnetic substorm that lasted for about 12 hours. The maximum value of the Kp index was 5 between 06h00 and 09h00 UT. At about the same time, the Dst index decreased gradually from -50 nT to ~ -80 nT between 12h00 and 15h00 UT and gradually recovered at about 18h00 UT. The E-fields reached a maximum value of ~ 5 mV/m. The average terrestrial wind speed was < 5 m/s. The solar wind fluctuated between ~ 330 to ~ 380 km/s throughout the day. The observed wave-like structures on 29 May 2010 coincided with the storm time, particularly when the Dst was ~ -80 nT. Therefore, the observed wave-like structures may have been associated with the storm activity that could also have enhanced the fluctuations in the E-field. Sub-/storms are known to induce changes in the electron density of the ionosphere and the process of adjusting to the changes manifests in the form of wave activity in the ionosphere. However, it should be noted that, as seen in the previously mentioned events, wave-like structures are also observed on geomagnetically quiet days.

4.3 Ionospheric oscillations and geomagnetic pulsations

Magnetic pulsations, also known as ultra low frequency (ULF - 1 mHz to 1 Hz (1 - 1 000 seconds)) waves, are as a result of a number of processes in the magnetosphere and solar wind. They fall into two categories, namely pulsations continuous (Pc) and pulsations irregular (Pi). Pc oscillations have quasi-sinusoidal waveforms while Pi oscillations have irregular waveforms. An increase in solar wind velocity, changes in the interplanatary magnetic field (IMF) and occurrence of a magnetospheric substorm or magnetic storm influence the type of ULF wave observed on Earth. The quasi-periodic variations in the solar wind density and dynamic pressure cause the magnetosphere to expand and contract, creating global changes in the interplanatary magnetic field (McPherron, 2005).

This section presents results of a cross-correlation between Doppler shift measurements and Pi2 pulsations in ground measurements of the geomagnetic field recorded in Hermanus. The Pi2 geomagnetic pulsations have periods of $\sim 1 - 3$ minutes and are known to cause ionospheric oscillations which sometimes appear as "saw-tooth"-shaped structures on the Doppler shift spectrograms. These oscillations have been observed to occur simultaneously on the three Doppler sounding signals. The ionospheric oscillations are attributed to the vertical movement of the ionospheric plasma which is associated with the $E \times B$ drift induced by the alternating electric field of an incident magnetohydrodynamic (MHD) wave (Chum *et al.*, 2009, and references therein). Sutcliffe and Poole (1989) show that these oscillations can also be associated with magnetic field variations and compression or rarefaction of the plasma by the wavefields. A comparison of ionospheric oscillations with ground measurements of magnetic pulsations has been discussed by several authors (e.g. Sutcliffe and Poole, 1989, 1990; Menk, 1992; Marshall and Menk, 1999; Waters *et al.*, 2007; Chum *et al.*, 2009). A cross-correlation analysis of Doppler shift records and irregular night-time Pi2 pulsations of the geomagnetic field has been done (Chum *et al.*, 2009, and references therein). This study concludes that the Doppler signals are usually best correlated with fluctuations of the horizontal components and the amplitude of the magnetic field.

For this study, fluctuations in the Pi2 frequency band were obtained by subtracting the running means computed over a period $T_p = 300$ s from individual signals. Thus, all fluctuations with $T_p > 300$ s were filtered. The fluctuations b_l of the B_l component at a time t_m were obtained from the following formula,

$$b_l(t_m) = B_l(t_m) - \frac{1}{N_p} \sum_{n=m+\frac{N_p}{2}}^{n=m-\frac{N_p}{2}} B_l(t_n) \tag{4.2}$$

where N_p is the number of samples in the time period T_p and T_p is centred around the time t_m (Chum *et al.*, 2009). Figure 4.14 shows Doppler shift spectrograms of ionospheric oscillations recorded on 7 October 2010 at 22h30 UT and 15 September 2010 at 21h15 UT. Table 4.1 shows the dates, periods of occurrence of the ionospheric fluctuations, the critical frequencies (foF2) and calculated peak heights (hmF2) of the F2 layer for the events in figure 4.14. The critical frequencies in both cases were lower than the sounding frequency (3.6 MHz) which indicates that reflections received were of R-X wave mode (Chum *et al.*, 2009, and references therein). Figure 4.15 shows a continuous wavelet transform (CWT) of the magnetic field amplitude, north-south and east-west components and Doppler shift records on 7 October 2010 at 22h30 UT and 15 September 2010 at 21h15 UT. These wavelet transforms were done by using complex Morlet wavelets. For both days the period of pulsation peaks around 2.5 minutes. For 7 October 2010 the pulsations in the east-west, north-south component and fluctuations in the magnetic field amplitude precede the Doppler shift. The peak in the east-west component pulsations observed between the 22^{nd} and the 24^{th} minutes of the CWT has a weak correspondence with the CWT of the Doppler signal. For 15 September 2010 the pulsations in the east-west, the north-south component, the magnetic field amplitude and the Doppler shift oscillations peak nearly at the same time (between 14 and 18 minutes). Figure 4.16 shows results of cross-correlation anal-

Table 4.1: Dates, periods of occurrence of the ionospheric fluctuations, the critical frequencies (foF2) and calculated peak heights (hmF2) of the F2 layer.

Date	Period (UT)	foF2(MHz)	hmF2(km)
07 October 2010	22h35 - 22h38	3.35	391.9
15 September 2010	21h17 - 21h35	3.48	329.8

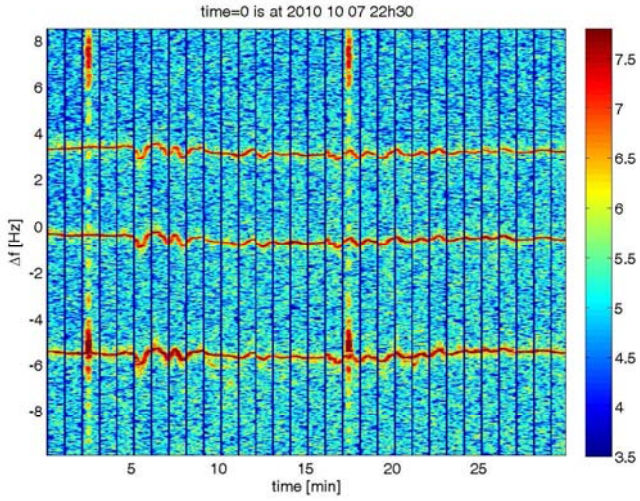

(a)

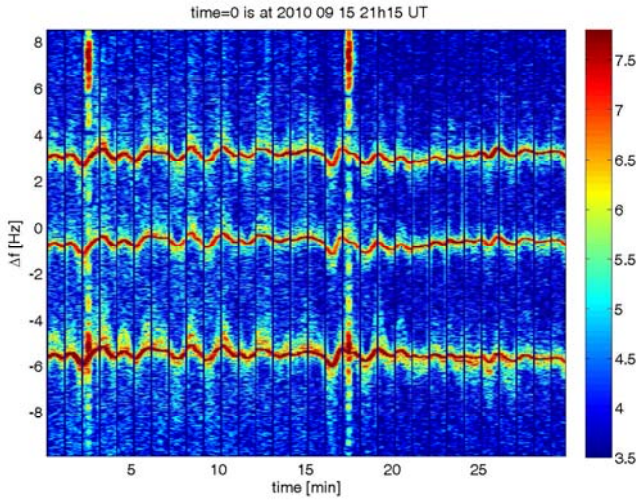

(b)

Figure 4.14: Examples of Doppler shift spectrograms showing ionospheric oscillations.

ysis of geomagnetic pulsations and ionospheric oscillations on 7 October 2010 at 22h30 UT and 15 September 2010 at 21h15 UT. The top panel shows fluctuations in the north-south (Bns), east-west components (Bew) and amplitude (B) of the magnetic field and Doppler shift (Doppler), while cross-correlation functions of the Doppler shift record and the magnetic field are shown at the bottom. For 7 October 2010 the cross-correlations of the Doppler signal with Bns, Bew and B are ~ -0.73, ~ -0.35 and ~ -0.55 for the time shifts 43, 40 and 30 s respectively.

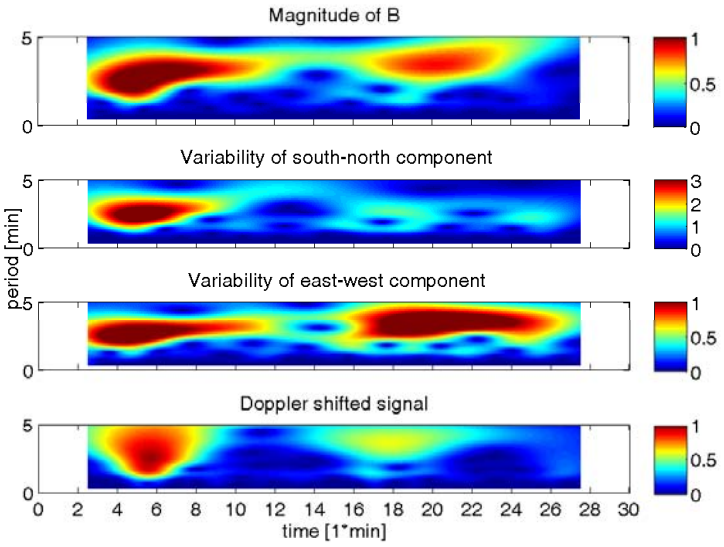

(a)

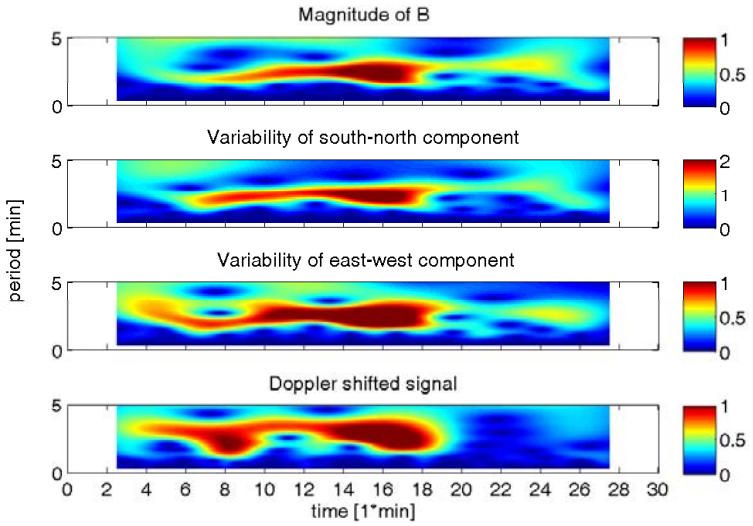

(b)

Figure 4.15: Continuous wavelet transforms (CWT) of the magnetic field amplitude and components and ionospheric oscillations measured by Doppler shift on (a) 7 October 2010 at 22h30 UT and (b) 15 September 2010 at 21h15 UT.

For 15 September 2010 the cross-correlations of the Doppler signal with Bns, Bew and B are ~ -0.53, ~ -0.581 and ~ -0.501 for the time shifts 88, 85 and 79 s respectively. For both days the ionospheric oscillations are neither in phase nor in anti-phase with the geomagnetic fluctuations.

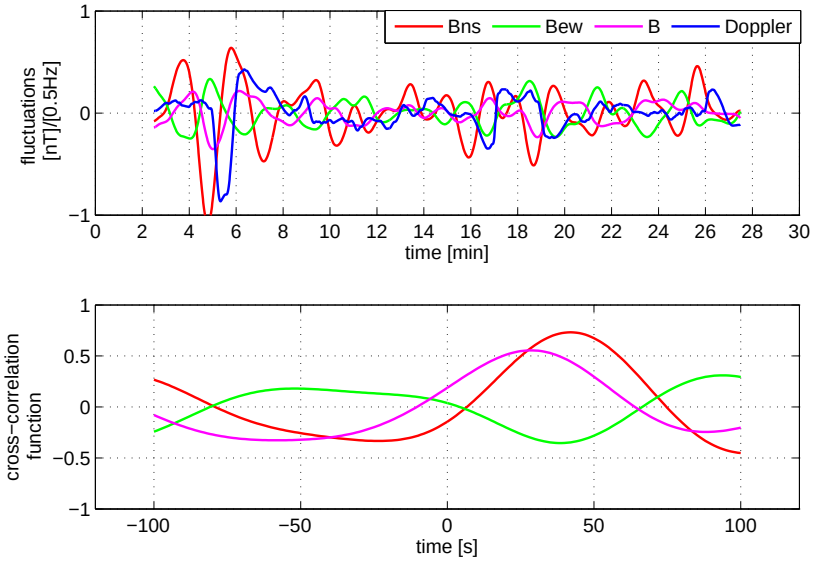

(a)

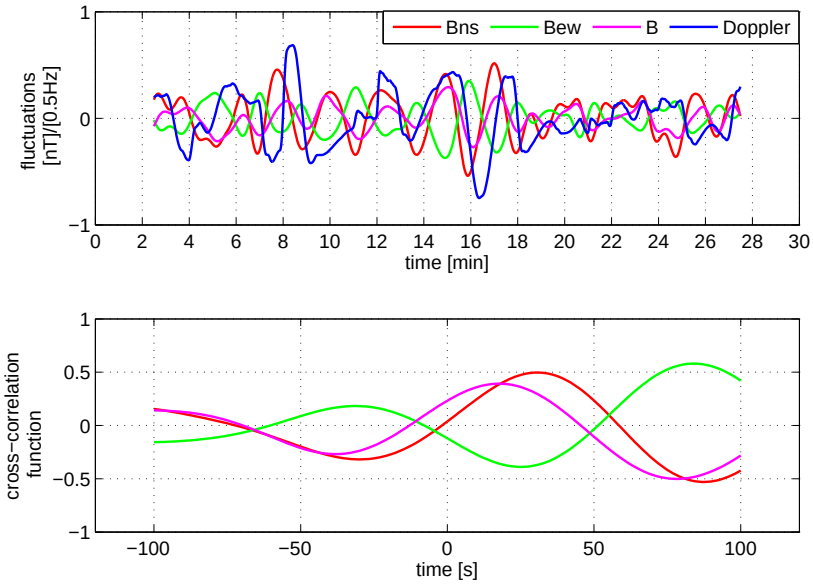

(b)

Figure 4.16: Top: fluctuations of Bns, Bew, B and Doppler shift. Bottom: cross-correlation functions of the Doppler shift record and magnetic field on (a) 7 October 2010 at 22h30 UT and (b) 15 September 2010 at 21h15 UT.

4.4 Doppler spread events

Doppler spread traces are observed when the Doppler signal is reflected by either a sporadic E or spread F layer and in some cases when a reflection of X-mode is received.

4.4.1 Doppler spread due to Doppler signal reflection by sporadic E layer

The cause, behaviour and diurnal variation of mid-latitude sporadic E (Es) are not fully understood, but are associated with thunderstorms, meteor showers, solar and geomagnetic activity. The wind shear theory explained by Whitehead (1989) gives an accredited description of the formation of mid-latitude Es. The vertical wind shears that contribute to the formation of the mid-latitude Es layers are associated with atmospheric tides and gravity waves (Laštovička, 2006, and references therein). Figure 4.17 shows examples of Doppler spread due to reflection by the Es layer. Such reflections can be received at any time of the day as long as $foEs > 3.6$ MHz. A reflection by the Es layer is analogous to a reflection by a spread F layer. The spread or diffuse signal is believed to be due to scattering by a distributed collection of relatively long-lasting small irregularities (Whitehead, 1989). Wave activity in the E and F region is not easily detected when a radio wave is reflected from the Es layer (Šindelářová *et al.*, 2008). Figure 4.18 shows ionograms recorded by the Hermanus ionosonde for the respective periods corresponding to events shown in figure 4.17. The Es layer was present during the entire hour for the 3 July, 20 June and 30 May 2010 events. On 25 June 2010 the Es layer was observed only between about 18h15 and 18h45 UT which corresponds to the period when the Doppler spread was observed. This implies that the signals received at these times were reflected by the Es layer.

4.4.2 Doppler spread due to Doppler signal reflection by a spread F layer

Figure 4.19 shows examples of Doppler spread as a result of a reflection from the spread F layer. Diffusion of the F layer is associated with a reflection of radio waves from ionospheric plasma irregularities and TIDs (Davies, 1989). Under spread F

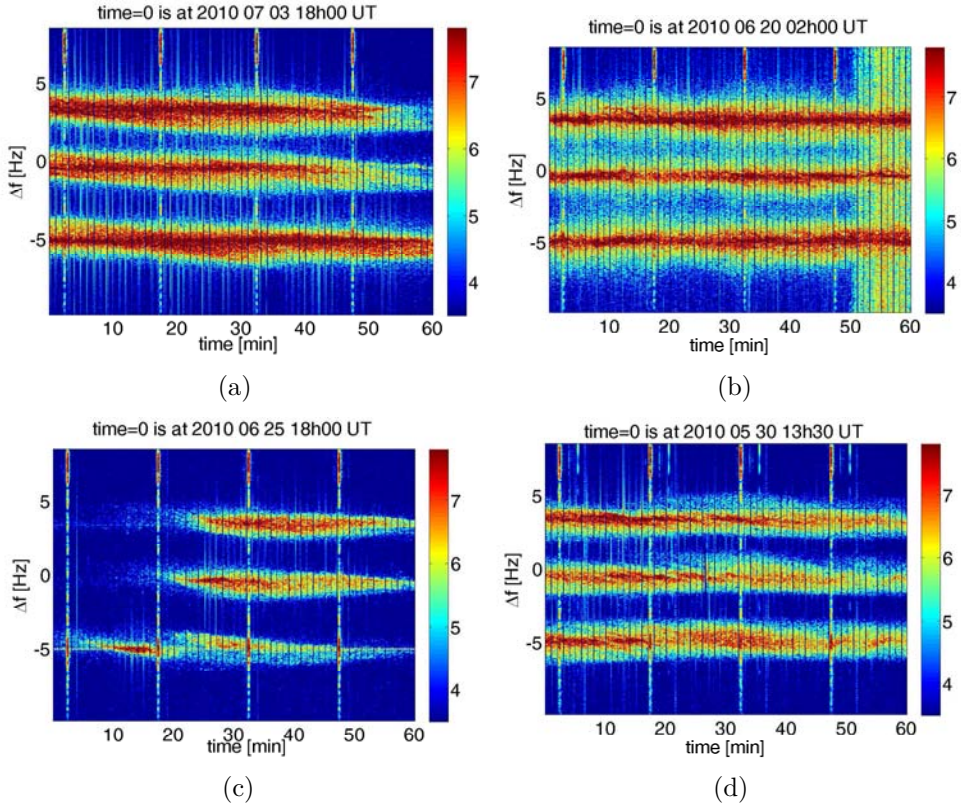

Figure 4.17: Doppler shift spectrogram showing Doppler spread due to reflection by the Es.

conditions, the trace becomes very diffuse and in some cases, a wave-like pattern is noticed in the diffused trace of the Doppler record (Ganti, 1975).

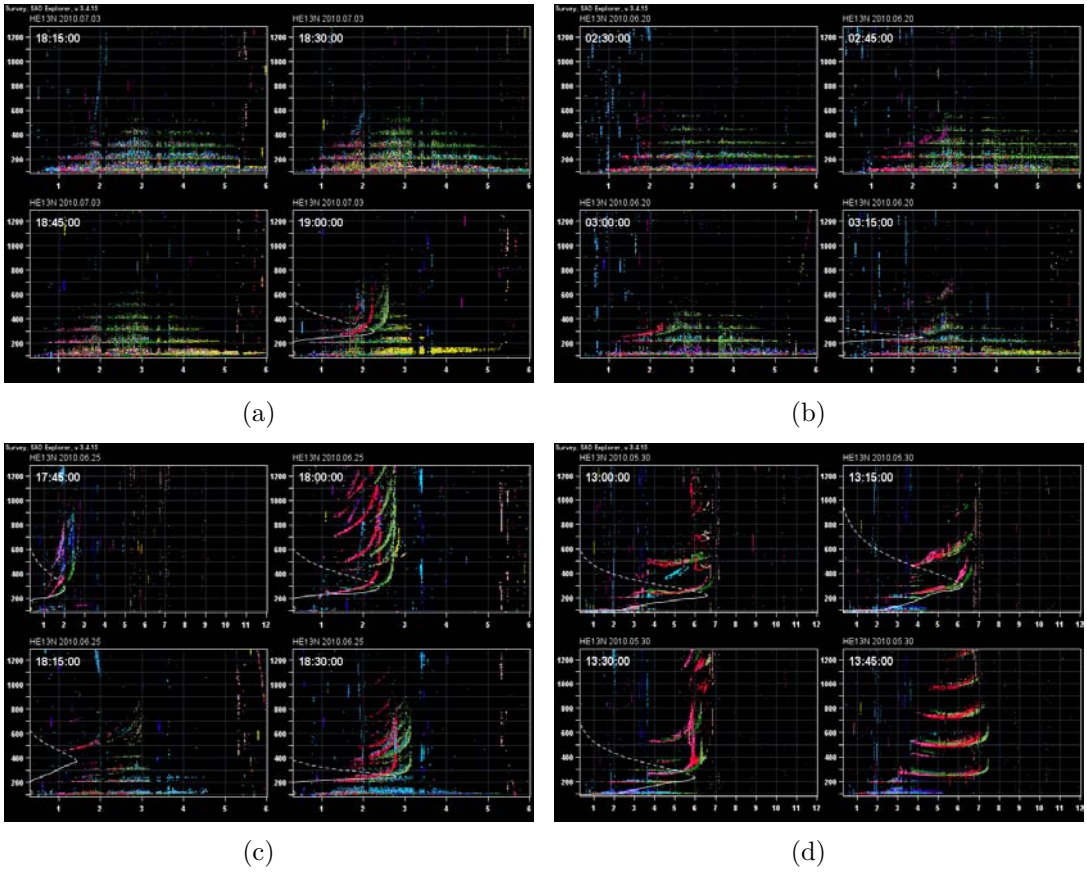

(a) (b)

(c) (d)

Figure 4.18: Ionograms for particular periods during May and June 2010 when Doppler spread was observed over Hermanus.

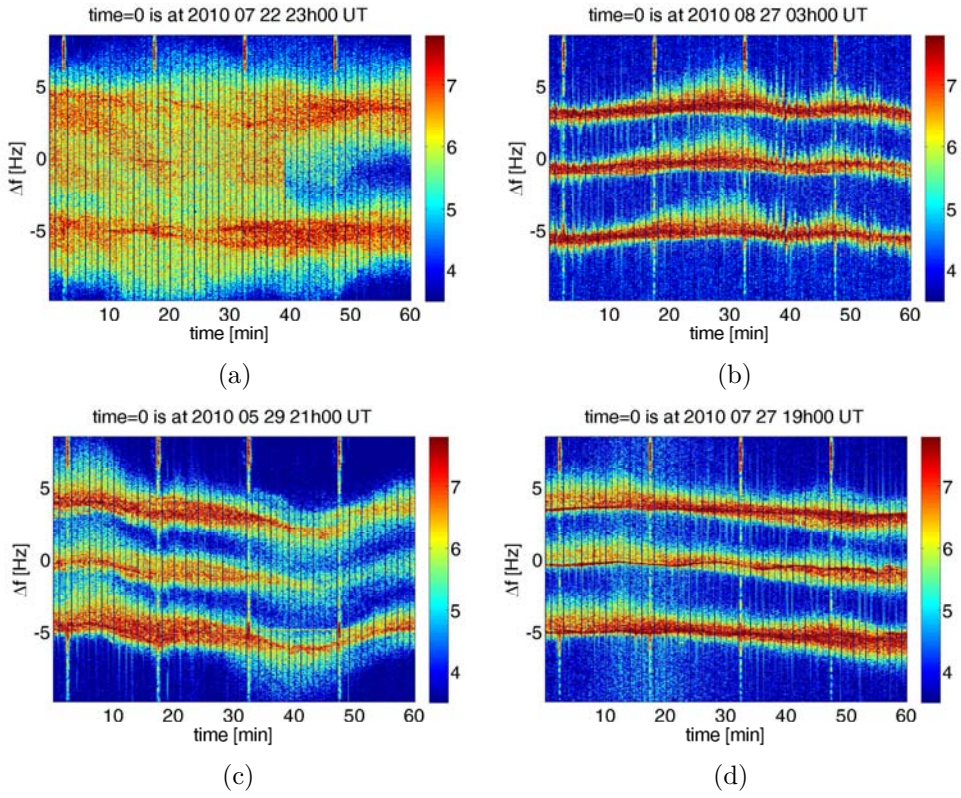

Figure 4.19: Examples of Doppler shift spectrograms showing Doppler spread due to radio signal reflection by a spread F layer.

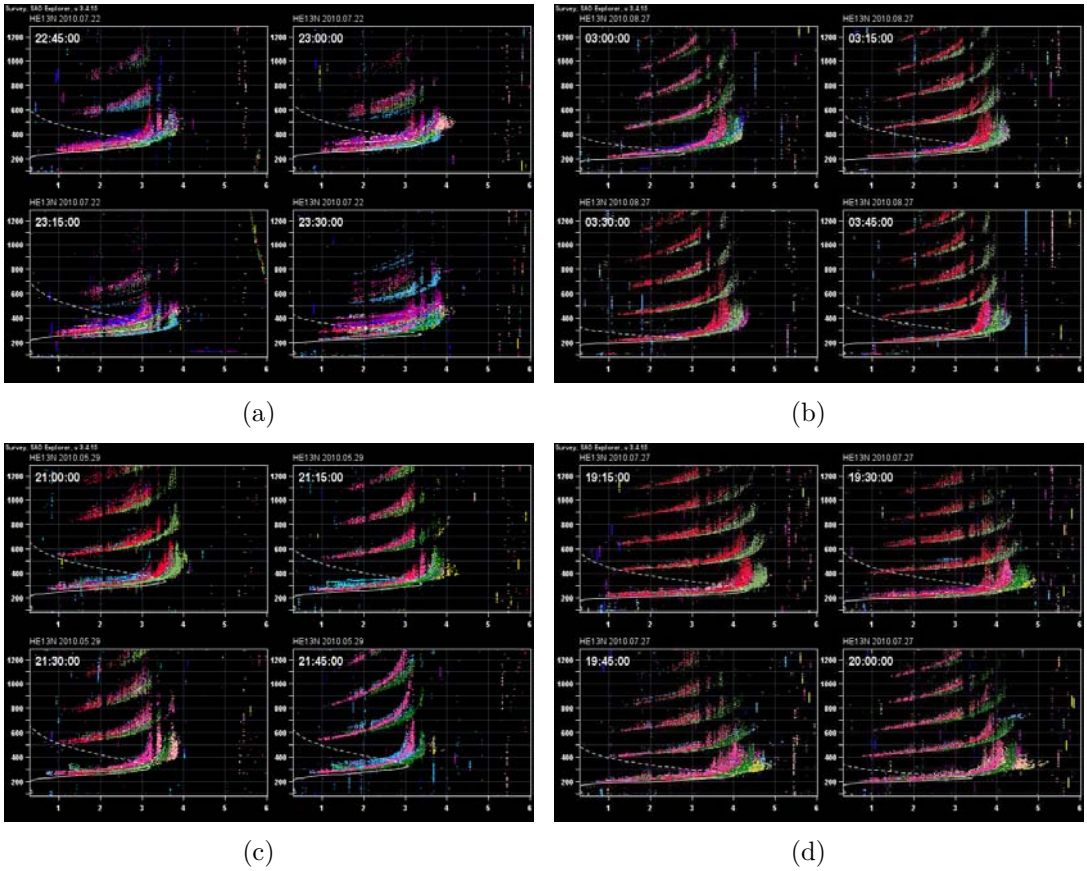

(a) (b)

(c) (d)

Figure 4.20: Examples for ionograms at periods corresponding to the spectrograms in figure 4.19.

Figure 4.20 shows ionograms for periods corresponding to the Doppler spread in figure 4.19. At heights corresponding to the Doppler sounding frequency (3.6 MHz), the F layer was diffuse. This implies that the reflections received by the Doppler radar receiver were from the spread F layer.

4.4.3 Doppler spread due to radio signal reflection of X-mode

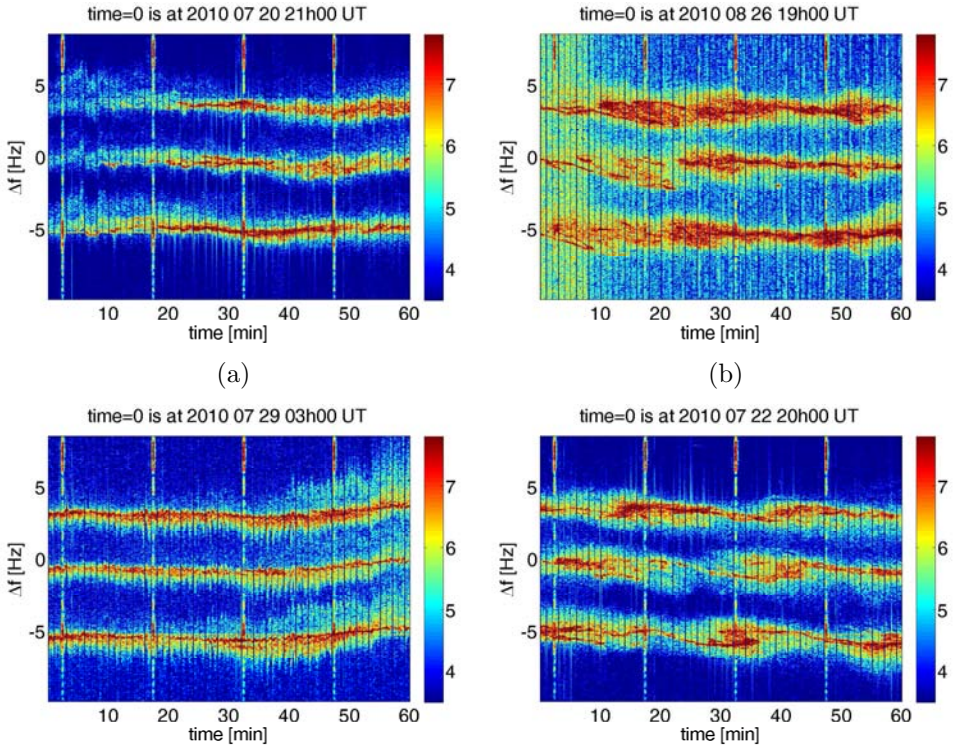

Figure 4.21: Examples of Doppler shift spectrograms showing Doppler spread due to radio signal reflection of X-mode.

If for some reason the ordinary ray is not visible, reflections of X-mode may be received. For example, when foF2 is slightly < 3.6 MHz and fxF2 $\gtrsim 3.6$ MHz, the signal is also reflected. This occurs mostly at night when foF2 decreases due to a decrease in the electron density which is a consequence of a reduction in photoionisation and continuation of the recombination process.

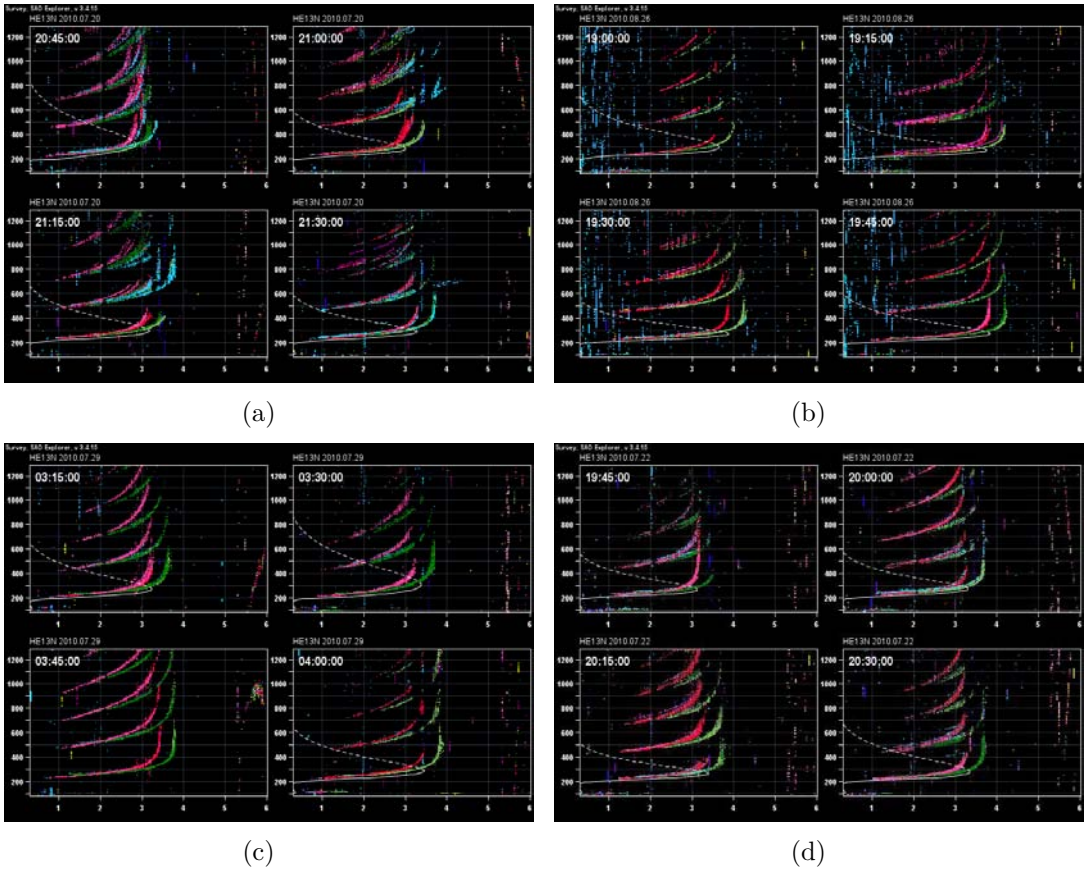

(a) (b)

(c) (d)

Figure 4.22: Examples of ionograms for periods corresponding to the spectrograms in figure 4.21.

Figure 4.22 shows ionograms for periods corresponding to the Doppler spread in figure 4.21. At heights corresponding to the Doppler sounding frequency (3.6 MHz), foF2 was < 3.6 while fxF2 was $\gtrsim 3.6$, yet the transmitted Doppler signal was reflected. This implies that the reflections received by the Doppler radar receiver were of the X-mode.

4.5 Sudden Frequency Deviation (SFD)

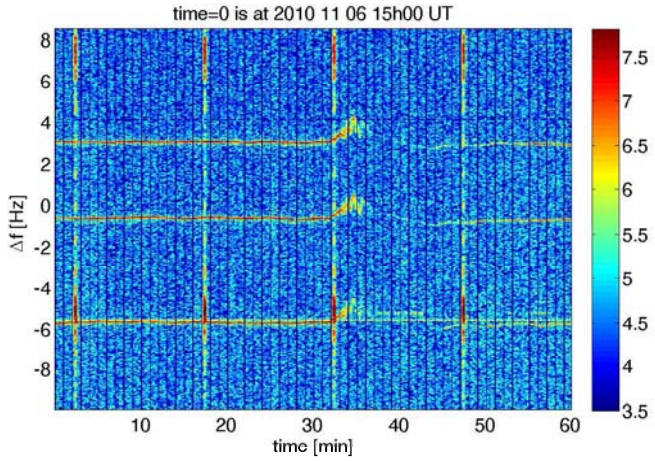

(a)

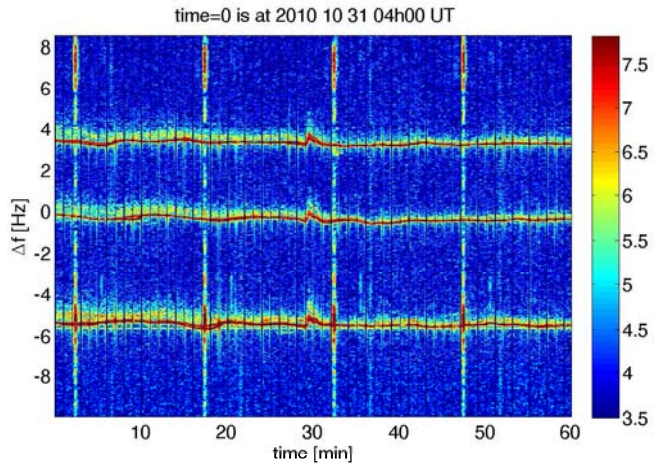

(b)

Figure 4.23: Doppler shift spectrogram recorded on (a) 6 November 2010 at 15h00 UT and (b) 31 October 2010 at 04h00 UT.

A few cases of SFD were observed. A SFD is an event in which the received frequency of a sky radio wave increases suddenly, peaks, and decays to the transmitted frequency (Donnelly, 1971). These frequency deviations are associated with solar flares, geomagnetic disturbances and TIDs. Solar flare-induced SFDs are attributed to the sudden short-lived increase in ionospheric ionisation as a consequence of the enhancement in the solar x-ray and UV emission. The change in the ionisation is proportional to the rate of change of the phase of the radio wave

frequency. The size and growth rate of the solar zenith angle, radiation enhancement, the path length and the transmitted frequency determine the magnitude of the SFD (Davies *et al.*, 1962). Though most of the observed SFDs are associated with solar flares, similar variations in frequency have been observed around periods of geomagnetic sudden commencements (Davies and Baker, 1966). In the event of a solar flare, there is a sudden displacement in the main trace while it shifts slowly with some additional spread trace during sudden commencement (Davies *et al.*, 1962). Figure 4.23 shows examples of SFD. On 6 November 2010 at about 15h36 UT there was a sharp increase in frequency at which time the onset of an M5.4 class solar flare was reported on *www.spaceweather.com*. Similarly, a sharp increase in frequency occurred on 31 October 2010 at about 04h30 and a C6 class flare was reported at 04h31 UT. In the latter case a sharp increase in frequency was observed near the start of the solar flare, followed by a sharp decrease and a recovery to the transmitted frequency.

4.6 Summary

In the case of wave-like disturbances, the time delay between instruments depends on the velocity and direction of the travelling disturbance and/or the source of the disturbance. In some instances, waves of certain periods may only be observed by the Doppler radar because of its high sensitivity to observe small disturbances that may be missed by the other instruments. It is important to also note the strength of the observed wave. This could be due to the difference in the operation and capabilities of the instruments. In most cases, the WT of the Doppler signal compares very well with the magnetic field pulsations of the H component. This agrees with Chum *et al.* (2009) who concluded that Doppler signals are usually best correlated with fluctuations of the horizontal components and the amplitude of the magnetic field. Cases of simultaneous observation of ionospheric fluctuations and magnetic pulsations could imply that either the latter led to the former or that both were induced by the same cause.

It is difficult to distinguish between Doppler spread due to the Es, spread F layer and X-mode by visual inspection. One can only be sure if the ionograms corresponding to the observed Doppler spread are examined for correlation. It should be noted that the condition for Doppler spread due to reflection from the Es and

spread F layer is always true, but it is not always the case for the X-mode, that is, not all reflections of X-mode correspond to a Doppler spread.

It is not easy to draw a definite conclusion from the cross-correlation between the ionospheric oscillations and geomagnetic pulsations, despite the fairly good cross-correlations obtained from the analysis. Though the CWT show that the ionospheric oscillations and geomagnetic pulsations peak either at the same time or at nearly the same time, the fact that it is difficult to identify whether the fluctuations presented in figure 4.24 are in phase or anti-phase at the periods considered makes it difficult to make an absolute conclusion. Most of the "ionospheric oscillation attributed to geomagnetic pulsation" events were only observed in September, October and November 2010.

Another important point is that for a particular observed event or signature no clear-cut conclusion of a definite source could be made. Rather it seemed that a joint contribution from all possible sources was the case. With the exception of the literature on SFD, no literature that attributed one particular cause could be found.

Chapter 5

Discussion and conclusion

In this chapter the results of this study are summarised and recommendations for future work are made. The aim of this project was to investigate the use of co-located radars and instruments to analyse ionospheric events over South Africa. It is hoped that the results of this project will improve the acquisition of data for space weather prediction purposes. The study of ionospheric events caused by space weather provides insight into the space environment that enhances the prediction of and preparation for space weather risks. It is for this reason that space scientists all over the world, including Africa, have embarked on a programme of acquiring instruments to obtain data for the study of ionospheric events. SANSA space science located in Hermanus, South Africa (34.4° S, 19.2° E) is one of the first observatories in Africa to host a co-located radar system which includes a DPS-4D digisonde, HF Doppler radar, GPS receiver and GPS scintillation receiver. These co-located radars and instruments in Hermanus were used for this study, offering the first results of the use of the HF Doppler radar. Recorded examples of ionospheric events are included. The magnitude and nature of the events vary, depending on their source, and were observed by all, some or at least one instrument. Using a co-located radar network provides the added advantage of always capturing events with at least one instrument.

5.1 Discussion

In this study ionospheric events were identified by visual inspection of the Doppler spectrograms. The events include wave-like structures, Doppler spread, sudden

frequency deviations and ionospheric oscillations associated with geomagnetic pulsations. Wave-like structures were most frequently observed, especially at sunset/sunrise during the winter months, compared to the other events. Georges (1968) observes and explains the seasonal variation in terms of mesospheric temperature changes which give rise to more gravity waves and therefore more wave-like structures in the reflected signal. Several authors observed the wave-like structures at sunrise and sunset (e.g. Davies and Baker, 1966; Šauli *et al.*, 2006; Chum *et al.*, 2010). The analysis of wave-like structures involved performing a wavelet transform of the Doppler signal, VTEC, magnetic field components and checking for scintillation events using the GISTM S_4 index. The wavelet transforms revealed wave activity in the Doppler signal, VTEC and fluctuations in the magnetic field components. In some cases, a wave of the same period could be observed in the wavelet transforms of the Doppler signal, VTEC and the magnetic field components but with a time delay. Chum *et al.* (2009) suggest that ionospheric oscillations induced by travelling disturbances are usually observed with time delays between different sounding points. It is important to note that, although a wave of a particular period observed in the Doppler signal was not observed in the other signals, there were waves of other periods observed by those instruments. For each event the solar wind speed, kp, terrestrial wind speed and E-fields were plotted and discussed. There were no scintillations corresponding to the observed wave-like structures on the dates of which the data was analysed. Considering the limited data coverage, the period of low solar activity and the fact that mid-latitude scintillations are rarely observed and are associated with the occurrence of magnetic storms, it may be incorrect to conclude that wave-like structures are not associated with scintillations (Basua *et al.*, 2002; Kintner *et al.*, 2007). Doppler spread events due to reflection by the sporadic E layer, spread F layer and reflections of X-mode are included. To differentiate these three, ionograms were checked and it was found that a Doppler spread corresponded to reflections by the sporadic E layer, spread F layer or reflections of X-mode. The ionograms for the period corresponding to a Doppler spread event are included. For cases in which Doppler spread is due to Es and spread F, the S_4 index was analysed and no scintillation events were observed for the period analysed.

Examples of sudden frequency deviation are included. Their occurrence was found to correspond to the onset of a solar flare. SFDs, described as a sudden sharp

increase in the main trace followed by a sharp decrease and a recovery, were also observed by Davies *et al.* (1962). There were not many of these events, probably because solar flares occur less often during a period of low solar activity, but as high solar activity approaches, more of these events can be expected. Cross-correlation analysis was carried out between ionospheric oscillations and geomagnetic pulsations, using software similar to that used by Chum *et al.* (2009). They obtained good cross-correlation results but noted that cross-correlation analysis could be misleading. However, in this study there were observations of simultaneous ionospheric oscillations and magnetic pulsations. Such ionospheric oscillations are said to be induced by ULF waves because of their high propagation velocities and relatively small distances to the sounding points (Chum *et al.*, 2009, and references therein).

5.2 Conclusions

Most event analyses of data produced by instruments such as ionosondes, GPS receiver and GISTM have been and still are based on the occurrence of magnetic storms and large scale TIDs. However, only small-/medium-scale TIDs were considered in this study. There were a few substorms during the period for which data was analysed. The state and dynamics of the upper atmosphere, especially the ionosphere, is influenced mainly by the sun. The fact that data analysis was done for a period of low solar activity may explain the absence of scintillation and instances where events recorded by the Doppler radar were not identified on data records from the other instruments. The analysis was done for data recorded between May and November 2010. This period is too short for a good statistical analysis and for absolute conclusions about the events and their causes, however, the feasibility of this kind of investigation was validated. It should be noted that for a particular observed event or signature, no single source could be identified as the sole originator. It seems that several sources played a joint role in the event. Except for literature on SFD, there appears to be no literature that attributes one particular ionospheric event to one particular cause.

5.3 Recommendations for future work

In this study data coverage was limited by the fact that the Doppler radar was installed towards the end of May 2010. In addition, the Doppler radar experienced a technical problem between December 2010 and mid-February 2011. For the sake of good statistical analysis and conclusive results, the data should cover a period longer than the period covered by this study. Also, the study was restricted to the Hermanus station. Future work should consider looking at a wider data coverage and including more stations in South Africa. Ionospheric events were inferred from observations made by the HF Doppler radar and then data recorded by the other instruments was analysed to check for correlation. Future work should consider doing a thorough analysis of data recorded by each of the radars and then noting correlations. In this way, events that are observed initially by a particular instrument can be identified, and this information will assist in determining the source and effect of the event.

References

Aquino M.H.O., Waugh S., Dodson A., Moore T. and Skone S., *GPS based Ionospheric Scintillation Monitoring*, Technical report, Institute of Engineering Surveying and Space Geodesy (IESSG), 2004.

Basua S., Grovesa K.M., Basu S. and Sultan P.J., "Specification and forecasting of scintillations in communication/navigation links: current status and future plans", *Journal of Atmospheric and Solar-Terrestrial Physics*, **64**, pp. 1745–1754, 2002.

Baumjohann W. and Treumann R.A., *Basic Space Plasma Physics*, Imperial College Press, 1997.

Beach L.T. and Kintner P.M., "Development and use of a GPS Ionospheric Scintillation Monitor", *IEEE transactions on Geoscience and Remote sensing*, **39(5)**, pp. 918–928, 2009.

Boska J., Šauli P., Altadill D., Sole G. and Alberca L.F., "Diurnal variation of the gravity wave activity at midlatitudes of the ionospheric F region", *Studia Geophysica et Geodaetica*, **47**, pp. 578–586, 2003.

Chum J., Hruška F., Burešová D., Šindelářová T., Hejda P. and Bochnicek J., "Ionospheric oscillations caused by geomagnetic Pi2 pulsations and their observations by multipoint continuous Doppler sounding; first results", *Advances in Space Research*, **44**, pp. 667–676, 2009.

Chum J., Laštovička J., Šindelářová T., Burešová D. and Hruška F., "Peculiar transient phenomena observed by HF Doppler sounding on infrasound time scales", *Atmospheric and Solar- Terrestrial Physics*, **70**, pp. 866–878, 2008.

Chum J., Šindelářová T., Laštovička J., Hruška F., Burešová D. and Baše J., "Horizontal velocities and propagation directions of gravity waves in the ionosphere over the Czech Republic", *Journal of Geophysical Research*, **115**(A11322), doi: 10.1029/2010JA015821, 2010.

Croom S.A., Robbins A.R. and Thomas J.O., "Variation of electron density in the ionosphere with magnetic dip", *Nature*, **185**, p. 902l, 1960.

Daglis I.A., *Effects of Space Weather on Technology Infrastructure*, Springer Science + Business Media, Inc, Greece, 2004.

Davies K., *Ionospheric Radio (Ionospheric Radio Wave Propagation)*, Boulder, Colorado, 1989.

Davies K. and Baker D.M., "On frequency variations of ionospherically propagated HF radio signals", *Radio Science*, **1**, pp. 545–556, 1966.

Davies K., Watts J.M. and Zacharisen D.H., "A study of F2 Layer Effects as Observed with a Doppler Technique", *Journal of Geophysical research*, **67**, pp. 601–609, 1962.

Dennison M. and Lorek C., *Radio Communication Handbook*, The Radio Society of Great Britain, England, 2005.

Donnelly R.F., "Extreme Ultraviolet Flashes of Solar Flares Observed via Sudden Frequency Deviations: Experimental results", *Solar Physics*, **20(1)**, pp. 188–203, 1971.

Farell J.A. and Barth M., *The Global Positioning System & Inertial Navigation*, McGraw-Hill, New York, 1998.

Ganti L.R., *Investigations of Atmospheric Dynamics using a CW Doppler Sounder array*, Technical report, The University of Alabama in Huntsville, 1975.

Gao Y. and Liu Z.Z., "Precise Ionosphere Modeling Using Regional GPS Network Data", *Global Positioning Systems*, **1(1)**, pp. 18–24, 2002.

Georges T.M., "HF Doppler studies of Travelling Ionospheric Disturbances", *Journal of Atmospheric and Terrestrial Physics*, **30**, pp. 735–746, 1968.

Goodman M.J., *Space weather & Telecommunications*, Radio propagation service, inc, New York, 2005.

GPSSiliconValley, *GPS Ionospheric Scintillation TEC Monitor*, 1131 Seena Avenue, Los Altos, CA 94024, USA, 2004.

Hines C.O., "Internal atmospheric gravity waves at ionospheric heights", *Canadian journal of Physics*, **38**, pp. 1441–1481, 1960.

Hofmann-Wellenhof B., Lichtenegger H. and Collins J., *GPS Theory and Practice*, Springer-Verlag Wien, New York, 1992.

Hunsucker R.D., "Atmospheric gravity waves generated in the high latitude ionosphere: A review", *Reviews of Geophysics*, **20**, pp. 293–315, doi:10.1029/RG020i00293, 1982.

Jacobs J. and Watanabe T., "Doppler Frequency Changes in Radio Waves Propagating Through a Moving Ionosphere", *Radio Science*, **1(3)**, pp. 257–264, 1966.

Kintner P.M., Ledvina B.M. and de Paula E.R., "GPS and ionospheric scintillation", *Space Weather*, **5**, pp. S09003, doi 10:1029/2006SW000260, 2007.

Laštovička J., "Forcing the ionosphere by waves from below", *Atmospheric and Solar- Terrestrial Physics*, **68**, pp. 479–497, doi: 10.1016/j.jastp.2005.01.018, 2006.

Lee D.T.L. and Yamamoto A., "Wavelet Analysis: Theory and Applications", *Hewlett-Packard*, pp. 44–52, 1994.

Marshall R.A. and Menk F.W., "Observations of Pc 3-4 and Pi 2 geomagnetic pulsations in the low-latitude ionosphere", *Annales Geophysicae*, **17**, pp. 1357–1410, 1999.

McNamara L.F., *The Ionosphere: Communications, Surveillance, and Direction Finding*, Krieger publishing company, Malabar, Florida, 1990.

McPherron R.L., "Magnetic pulsations: their sources and relation to solar wind and geomagnetic activity", *Surveys in Geophysics*, **26**, pp. 545–592, 2005.

Menk F.W., "Characterization of ionospheric Doppler oscillations in the Pc3-4 and Pi2 magnetic pulsation frequency range", *Planetary space Science*, **40**, pp. 459–507, 1992.

Millward G.H., Rishbeth H., Fuller-Rowell T.J., Aylward A.D. and Quegan S., "Ionospheric F2 layer seasonal and semiannual variations", *Geophysical Research*, **101**(A3), pp. 5149–5156, 1996.

Misisti M., Misiti Y., Oppenheim G. and Poggi J., *Wavelet Toolbox 4 (User's Guide)*, The Math Works, Inc, Natick, 2009.

Morton Y.T. and Mathews J.D., "Effects of the 13-14 March 1989 geomagnetic storm on the E-region Tidal Ion Layer structure at Arecibo during AIDA", *Journal of Atmospheric and Terrestrial Physics*, **55(3)**, pp. 467–489, 1993.

Nahayo E., *Magnetic Results 2009 Hermanus, Hartebeesthoek and Keetmanshoop observatories*, Technical report, Hermanus Magnetic Observatory, Hermanus, South Africa, 2009.

Nasyrov G.A., "Variations in the atomic oxygen 630 nm emission intensity related to orography", *Geomagnetism and Aeronomy*, **49**, pp. 528–531, 2009.

NAVSTARGPS, *Navigation Signal Timing and Ranging (NAVSTAR) GPS user equipment introduction (Public Release Version)*, 1996.

Opperman B.D., Cilliers P.J., Mckinnell L.A. and Haggard R., "Development of a regional GPS-based ionospheric TEC model for South Africa", *Advances in Space Research*, **39**, pp. 808–815, 2007.

Opperman B.D.L., *Reconstructing Ionospheric TEC over South Africa using Signals from a regional GPS network*, Ph.D. thesis, Rhodes University, 2007.

Reinisch B.W., Galkin I.A., Khmyrov G., Kozlov A. and Kitrosser D.F., "Automated collection and dissemination of ionospheric data from the digisonde network", *Advances in Radio Science*, **2**, pp. 241–247, 2004.

Richards J.A., *Radio Wave Propagation (An Introduction for the Non-Specialist)*, Springer-Verlag Berlin Heidelberg, Canberra, Australia, 2008.

Rishbeth H. and Garriot O.K., *Introduction to Ionospheric Physics*, volume 14 of *"International Geophysics"*, Academic Press, 1969.

Šauli P., Abry P., Altadill D. and Boska J., "Detection of the wave-like structures in the F-region electron density: Two station measurements", *Studia Geophysica & Geodaetica*, **50**, pp. 131–146, 2006.

Sauli P. and Boska J., "Tropospheric events and possible related gravity wave activity effects on the ionosphere", *Journal of Atmospheric Solar Terrestrial Physics*, **63**, pp. 945–950, 2004.

Schaer S., *Mapping And Predicting the Earth's Ionosphere Using the Global Positioning System*, Ph.D. thesis, Astronomical Institute, University of Berne, Berne, Switzerland, 1999.

Seybold J.S., *Introduction to RF propagation*, John Wiley & Sons, inc, Hoboken, New Jersey, 2005.

Šindelářová T., Burešová D. and Chum J., "Observations of Acoustic Gravity Waves in the ionosphere generated by severe tropospheric weather", *Studia geodesica & geodaetica*, **53**, pp. 403–418, 2009.

Šindelářová T., Burešová D., Chum J. and Hruška F., "Doppler observations of infrasonic waves of meteorological origin at ionospheric heights", *Advances in Space Research*, **43**, pp. 1644–1651, 2008.

Sizun H., *Radio Wave Propagation for telecommunication Applications*, Springer-Verlag Berlin Heidelberg, New York, 2005.

Spogli L., Alfonsi1 L., Franceschi1 G.D., Romano1 V., Aquino M.H.O. and Dodson A., "Climatology of GPS ionospheric scintillations over high and mid-latitude European regions", *Annales Geophysicae*, **27**, pp. 3429–3437, 2009.

Sutcliffe P.R. and Poole A.W.V., "Ionospheric Doppler and electron Velocities in the presence of ULF waves", *Geophysical Research*, **94**, pp. 13,505–13,514, 1989.

Sutcliffe P.R. and Poole A.W.V., "The relationship between ULF geomagnetic pulsations and ionospheric Doppler oscillations: model predictions", *Planetary Space Science*, **38**, pp. 1581–1589, 1990.

Torrence C. and Compo G.P., "A practical guide to Wavelet Analysis", *American Meteorological Society*, pp. 61–77, 1998.

Vadas S.L. and Fritts D.C., "Thermospheric responses to gravity waves arising from mesoscale convective complexes", *Journal of Atmospheric Solar Terrestrial Physics*, **66**, pp. 781–804, doi:10.1016/j.jastp.2004.01.025, 2004.

Walterscheid R.L. and Hickey M.P., "Acoustic waves generated by gusty flow over hilly terrain", *Journal of Geophysical Research*, **110**, doi: 10.1029/2005JA011166, 2005.

Waters C.L., Yeoman T.K., Sciffer M.D., Ponomarenko P. and Wright D.M., "Modulation of radio frequency signals by ULF waves", *Annales Geophysicae*, **25**, pp. 1113–1124, 2007.

Wernik A., *What is Space Weather?*, Technical report, Polish Academy of Sciences, 2005.

Whitehead J.D., "Recent work on mid-latitude and equatorial sporadic E", *Atmospheric and Terrestrial Physics*, **51**, pp. 401–424, 1989.

Williamson S.P., Bonadonna M.F. and Babcock M.R., *The National Space Weather Program: 2010 and the Next Decade*, Technical report, NASA, Federal Coordinator for Meteorological Services and Supporting Research, 2010.

Zandt T.E.V. and Knecht R.W., *The structure and physics of the atmosphere, in Space Physics*, R. John Wiley, New York, 1964.